**UNIVERSITY OF OSLO**
**Department of Physics**

# Investigation of zinc vacancies and their influence on N and Li related defect complexes in hydrothermal ZnO

Master thesis

Knut Erik Knutsen

**1. June 2009**

**Abstract**

Hydrothermal ZnO samples having lithium concentration in the range of $3 \times 10^{14}$ – $1 \times 10^{17}$ Li/cm$^3$ were implanted with nitrogen. The variation of Li concentration was done by high temperature pre-anneals and controlled by secondary-ion mass spectrometry (SIMS). The efficiency of zinc vacancy clustering after ion implantation and post-implantation anneals was monitored by positron annihilation spectroscopy (PAS). It was found that the presence of Li enhances clustering of zinc vacancies considerably. In addition the resistivity evolution was monitored by scanning spreading resistance microscopy, and in combination with PAS, the results indicate the presence of a Li–N related doubly negative complex emerging at 800 °C. SIMS has also revealed the presence of additional processing induced defects acting as a Li traps with much lower diffusivity than untrapped Li.

# Acknowledgements

First I would like to thank my supervisor Prof. Andrej Yu. Kuznetsov for pointing me in the right direction, and introducing me to the rich field of defects in ZnO. His unmatched enthusiasm and his belief in my work has been of great help.

Thanks to Dr. Asier Zubiaga for introducing me to PAS, and for helping me out with my measurements in Helsinki. He and Dr. Filip Tuomisto was of great help when I was struggling to understand my PAS results. Thanks to Dr. Lasse Vines for teaching me the basics of how to operate the SIMS, and for helping me measure my samples. Thanks also for patiently answering my many questions. Thanks to Klaus Magnus Johansen for his critical mind which triggered fruitful discussions and for proof reading my thesis. Thanks to Viktor Bobal for his help with ion-implantation and for answering any questions about equipment in the cleanroom. Thanks to my fellow students Chi Kwong Tang and Jonathan Polfus for discussions regarding all from physics to typesetting in LaTeX to music and films. Thanks to my "room mates" and all my other colleagues at the MiNa lab for creating a friendly environment to work in.

I would like to thank my parents for supporting my decisions and for telling me that hard work opens more opportunities.

Most importantly, I would like to thank my dear Christine for her support and for encouraging me to keep going even when motivation failed. And for making me remember that life outside the university makes it all meaningful.

# Contents

# Chapter 1

# Introduction

Semiconductors is a cornerstone of our modern information society. In particular silicon technology and its exponential growth has had a huge impact on many parts of society. Silicon is used in all kinds of modern electronic devices like computers, mobile phones and washing machines. Although silicon has some great advantages over other semiconductors, in particular its native oxide and the passivation thereof, it also lacks some important properties. Among these are a direct bandgap which is needed for optoelectronic purposes. Zinc oxide is a wide bandgap semiconductor ($\sim$3.37 eV) which has received a great deal of attention during recent years. This is due to the properties of ZnO compared to other wide bandgap semiconductors like GaN, its commercial "competitor". High exciton energy is one of these important properties which makes ZnO a potential material for optoelectronic devices like room temperature exciton lasers [1,2]. The wide bandgap of ZnO is tunable by alloying with for example Cd or Mg [3, 4], allowing different wavelength LEDs in the blue to ultraviolet region. Solar cells is another application in which ZnO may become important, either as an active layer in a multi-junction solar cell, or as a transparent conductive oxide on crystalline silicon solar cells. It has also been theoretically suggested that ZnO doped with transition metals has a high Curie temperature [5]. This makes ZnO a candidate for spintronics ap-

plications where both the electron charge and spin can be utilized to carry information. In addition, cheap ZnO substrates grown by hydrothermal (HT) method are available. Importantly the HT method is scalable and thus ZnO is very well suited for large volume production. However, a bottleneck for the ZnO technology is insufficient reliability of *p*-type doping, which is needed to manufacture *pn*-junctions — fundamental components to most of the electronic applications.

Group-V elements — N, P, and As — have been suggested to work as acceptors, substituting oxygen in ZnO. N has been the most promising. Group-I elements — Li, Na and K — on Zn site have been suggested as shallow acceptors, but Li in particular has the problem of being compensated by Li on interstitial site acting as a donor [6].

Doping of semiconductors is often done post-growth by in-diffusion of dopants or ion-implantation. The latter method has the side effect of creating high concentrations of point defects in the material. To remove defects and activate dopants, annealing is required and the effects of annealing at different temperatures can be quite complex. Furthermore the dopants themselves can modify the behavior of intrinsic defects like vacancies and interstitials [7], of which some are electrically active in ZnO. Since ZnO is naturally *n*-type, it is obvious to ask which defect is the dominant donor, but the answer is still controversial after numerous studies [8, 9, 10]. In addition HT ZnO contains impurities like Li, Mg and Cu, which properties need to be understood in order to utilize HT ZnO in optoelectronics. In particular Li is important because of its amphoteric nature in ZnO [6], making it responsible for high resistive as-grown substrates. Vacancy clusters has been shown to deactivate Li compensators in ZnO, thus proving a correlation between Li and zinc vacancies [11]. In $N^+$ implanted HT ZnO acceptor activation has been observed, though it is uncertain whether N or Li is responsible [12]. Co-doping thin film ZnO with Li and N has been shown to produce stable *p*-type material, where a Li–N complex is found to be the responsible acceptor [13, 14, 15].

The aim of this thesis is to clarify the role of Li on evolution of radiation induced defects in ZnO by $N^+$ ion-implantation. In addition, possible activation of N and Li related acceptors in ZnO will be investigated.

# Chapter 2

# Background

This chapter describes basic semiconductor theory including crystals and crystal defects. Some of the previous work done on identifying defects responsible for making as-grown ZnO *n*-type is presented, along with the work on doping of ZnO to achieve *n*- or *p*-type conductivity. A particular weight is given to literature on ZnO doped with N and/or Li, and on characterization of acceptor type vacancies related to the dopants and doping method by positron annihilation spectroscopy (PAS).

The first section of this chapter uses information found in coursebooks on Solid State Physics by Kittel [16] and Solid State Electronic Devices by Streetman and Banerjee [17], and further in-depth literature can be found there.

## 2.1 Semiconductor Theory

A semiconductor, as the name suggests, has some properties between an electrical insulator and conductor. To explain this we first look at a crystalline solid, which is made up by a periodic arrangement of atoms. In an atom, the electrons can only occupy discrete levels of energy, and since electrons are fermions, they cannot occupy the same state as another electron, according to the Pauli principle. When several atoms forms a crys-

talline solid, these energy levels becomes energy bands, and the forbidden gap between them is called the bandgap ($E_g$). The differences between metals, semiconductors and insulators are illustrated in Figure 2.1. In

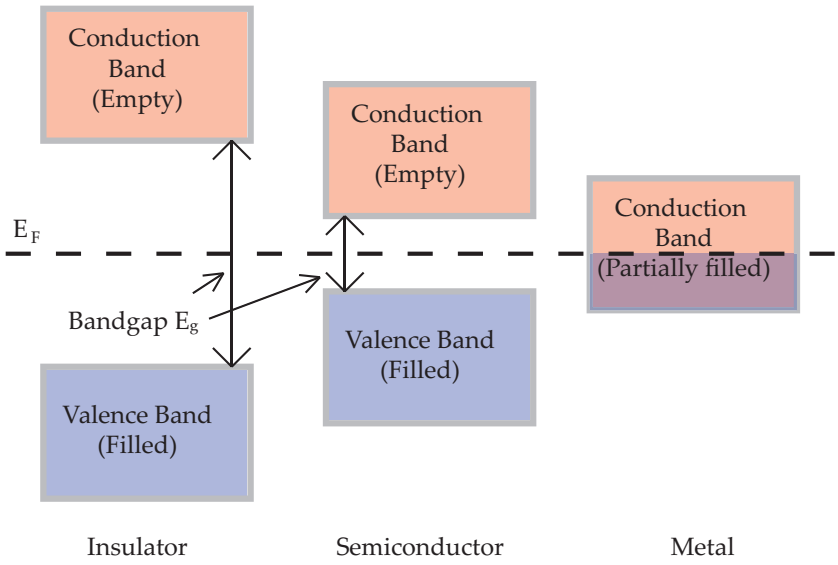


Figure 2.1: *Schematics of the energy band structure in solids, illustrating the difference between insulators, semiconductors and metals.*

metals, the energy states in the conduction band are partially filled with electrons and thus the electrons are able to move freely to empty states. In an insulator the valence band is completely filled with electrons, so that no empty states exist for the electrons to move into. The conduction band contains empty states, but no electrons. Thus no net transport of charge is possible. Semiconductors are in this respect similar to insulators. The difference is that the bandgap of semiconductors is smaller than that of insulators. At 0 K a semiconductor is insulating, and as temperature increases, thermally excited electrons jump across the bandgap. One such event creates an electron in the conduction band, and a hole in the valence band, together called an electron-hole pair. Both of these can conduct electricity. A way to control the conductivity of semiconductors is to introduce electrons or holes through a process called doping. By this technique con-

ductivity can be varied over several orders of magnitude. An example is silicon (Si), a group IV element, meaning it has 4 valence electrons. When many Si atoms are brought together to a solid it forms covalent bonds to 4 other Si atoms which forms a tetrahedron around it and builds a diamond structure. If no impurities are present, the perfect Si crystal is called an intrinsic semiconductor. If an atom with 3 valence electrons (group III elements) substitutes a Si atom, there are too few electrons to form bonds with all the surrounding Si atoms, and if the energy level of this unfilled state is close to the valence band, it will be filled by an electron from the valence band and thus a hole is created in the valence band. A similar mechanism can be described when atoms with 5 valence electrons (group V elements) are substituting Si. It then adds electrons to the conduction band. These dopants are called *p*- and *n*-type, respectively.

The charge carriers in a solid, electrons and holes, obey Fermi-Dirac statistics. As more electrons are added to the system, they will have to occupy higher and higher states of energy. The probability of a state being occupied by an electron is described by the Fermi-Dirac distribution function:

$$f(E) = \frac{1}{1 + e^{(E-E_{\mathrm{F}})/\mathrm{k}T}} \tag{2.1}$$

In this equation, $E_{\mathrm{F}}$ is the Fermi level and is defined as the energy at which a state has probability $1/2$ of being occupied. $T$ is absolute temperature and k is the Boltzmann constant. At 0 K the distribution function is zero above the Fermi level and 1 below the Fermi level. When temperature is increased, some of the available states in the conduction band are occupied and the shape of the distribution function changes, but it remains symmetrical around the Fermi level, see Figure 2.2. This symmetry makes the Fermi level a natural point of reference for calculating carrier concentrations in semiconductors.

The band structure of a semiconductor is very important for the semiconductors optical properties. The bandgap can be direct or indirect. To explain this further we need to move into reciprocal space. Any periodic

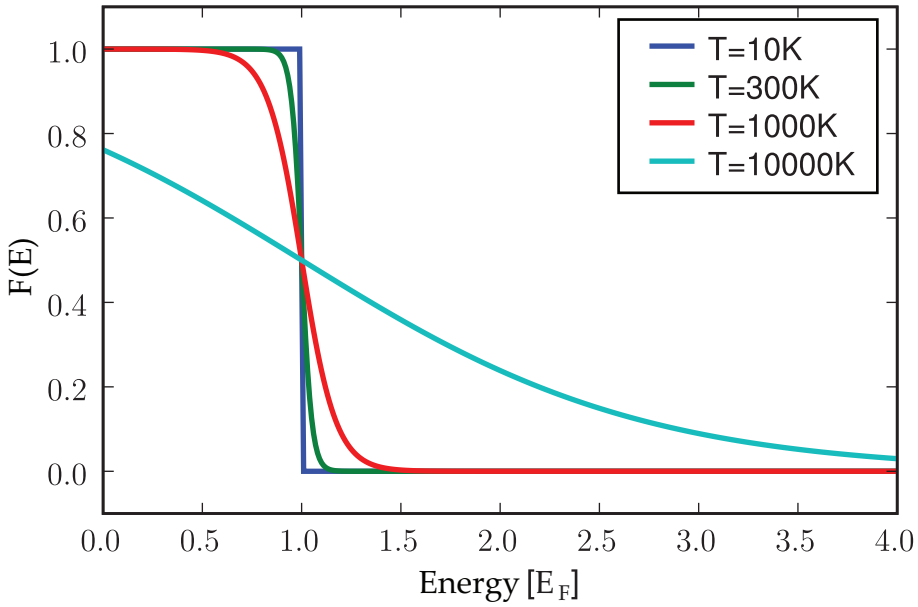


Figure 2.2: *Fermi-Dirac distribution as a function of energy at different temperatures. The energy is in units of Fermi energy.*

lattice can be transformed into a reciprocal lattice by a Fourier transform. A vector in reciprocal space has units of inverse length and can be described as a wave vector $\vec{k}$. In reciprocal space ($\vec{k}$-space), energy can be plotted as a function of the wave vector and provides a map of allowed values of energy as seen in Figure 2.3. In a direct bandgap semiconductor, the top of the valence band is at the same point in $\vec{k}$-space as the bottom of the conduction band. An electron in the conduction band may cross the bandgap to recombine with a hole in the valence band. During recombination, light is emitted. In an indirect semiconductor, the top of the valence band is at a different point in $\vec{k}$-space than the bottom of the conduction band, thus making a direct transition impossible. A recombination in an indirect semiconductor happens via phonons, resulting in a less probable transition. This mechanism leads to heat being created in the lattice rather than light emission as is the case in a direct semiconductor.

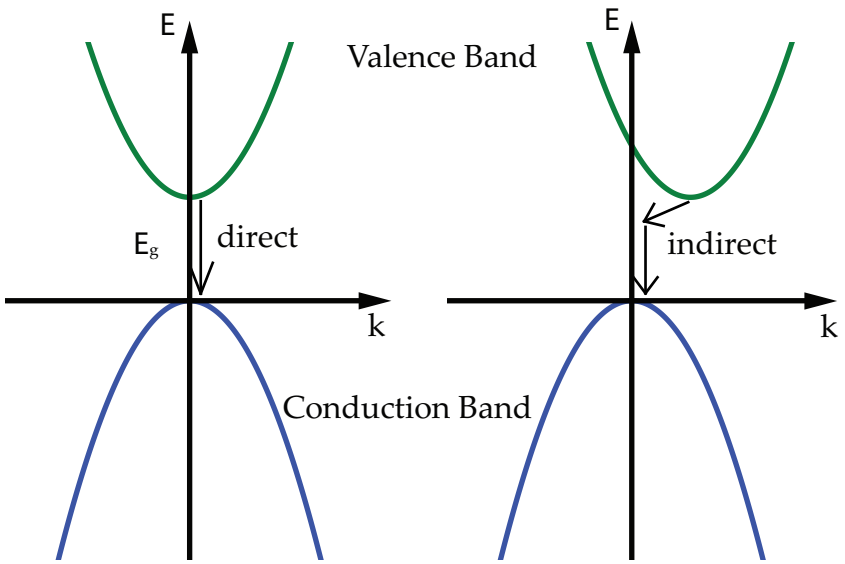


Figure 2.3: *Schematics illustrating the difference between direct (left) and indirect (right) bandgaps.*

### 2.1.1 Crystal Defects

Understanding defects is a vital part of semiconductor science. Defects can be an unintentional result of synthesis and processing, or a method of controlling electrical properties. Although defects can be of higher dimensions (line dislocations, plane dislocations *etc.*), the focus herein will be on point defects (0-Dimensional). Point defects can be of both intrinsic and extrinsic nature. Vacancies and self-interstitials are examples of intrinsic defects, while substitutional or interstitial impurities are examples of extrinsic defects. An illustration can be seen in the 2D crystal in Figure 2.4. These individual point defects may also agglomerate and form second phase particles, defect complexes or vacancy clusters. Intrinsic defects are formed from the constituents of the host material. For example, an interstitial is an atom which is not on its usual lattice position, but on a site between normal lattice positions. In ZnO intrinsic interstitials can be made of oxygen and zinc, $O_i$ and $Zn_i$, respectively. Similarly, a vacancy is a missing atom in the lattice, and in ZnO these are vacancies in oxygen

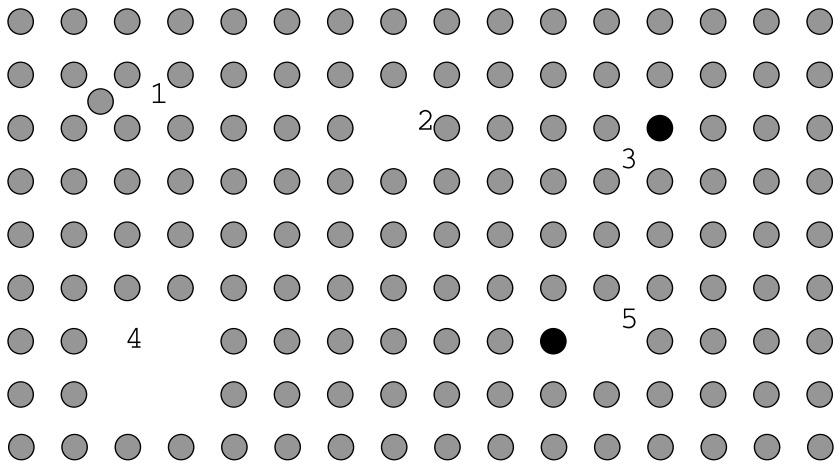


Figure 2.4: *Two dimensional crystal with different types of point defects. 1: self-interstitial, 2: vacancy, 3: substitutional, 4: vacancy cluster, 5: substitutional—vacancy complex*

and zinc sub-lattices, $V_O$ and $V_{Zn}$, respectively. An intrinsic substitutional defect cannot exist in elemental semiconductors like Si, but in ZnO, which is a compound semiconductor, it can. Such defects are called anti-sites and consist of intrinsic atoms in the wrong sub-lattice. Zinc on oxygen site and vice versa, $Zn_O$ and $O_{Zn}$, respectively. Extrinsic defects or impurities are atoms foreign to the host material. It can be any atom from the periodic system, but not all are electronically active in a given semiconductor. Impurities can be on substitutional sites, interstitial sites or be a part of larger complexes involving other intrinsic or extrinsic defects.

## 2.2 Properties of ZnO and previous work

### 2.2.1 Crystal structure

ZnO crystallizes in a hexagonal wurtzite structure and the unit cell has dimensions $a = 3.25\,\text{Å}$ and $c = 5.207\,\text{Å}$. The zinc atoms lie inside an imperfect tetrahedron of oxygen atoms, where the bond along the *c*-axis is shorter than the others as illustrated in Figure 2.5. This makes ZnO a po-

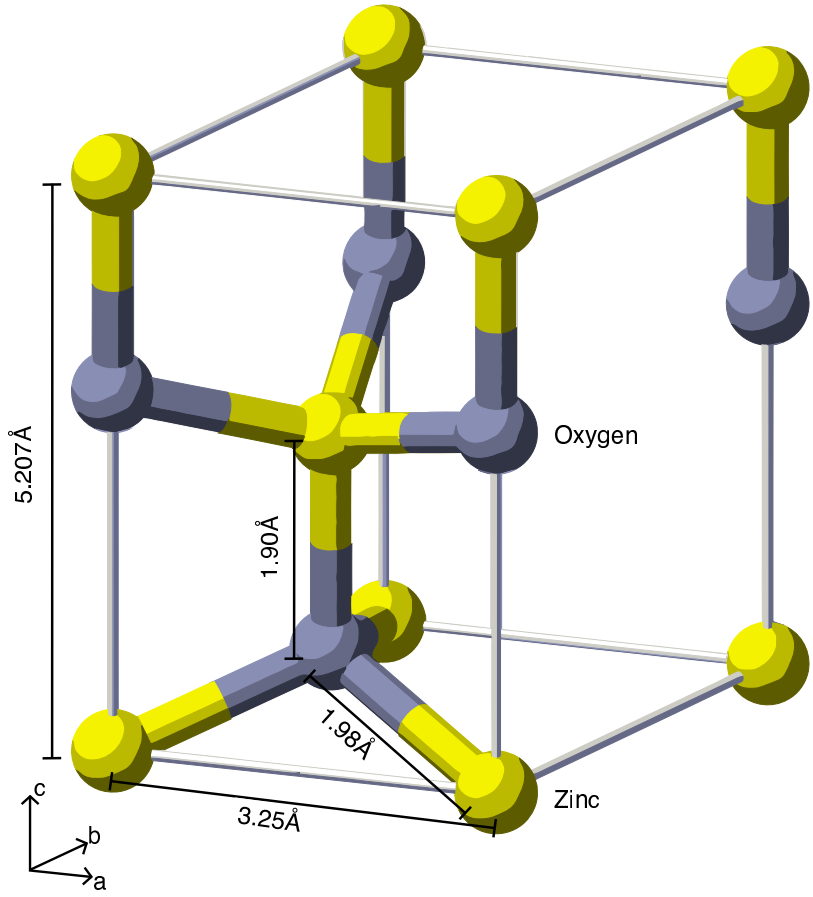


Figure 2.5: *Wurtzite structure unit cell. Space group $P6_3mc$*

lar or piezoelectric material along the *c*-axis. The $(000\bar{1})$ plane is called O-face because it is usually terminated with O, and similarly the (0001) plane is called the Zn-face. The polarity of the material can affect diffusion of dopants due to, for example, charge difference in the distribution.

### 2.2.2 Properties of intrinsic defects in ZnO

ZnO without any intentional doping usually exhibit an *n*-type conductivity. Many studies have been performed to determine the source of the *n*-type behaviour and there is still a significant controversy with this issue. Anyhow, a predominant concentration of donor-like intrinsic defects is one of the explanations.

Table 2.1: *Energy levels of intrinsic defects in ZnO. $E_c$ and $E_v$ are the conduction band edge and the valence band edge, respectively.*

| Defect | Energy level [meV] |
|---|---|
| $V_O$ | $E_c-100$ [18] |
| $Zn_i$ | $E_c-30$ [8] |
| $V_{Zn}$ | $E_v+270$ [19] |
| $O_i$ | deep acceptor [20] |
| $Zn_O$ | shallow donor [20] |
| $O_{Zn}$ | deep acceptor [20] |

$V_O$ and $Zn_i$, with energy levels as listed in Table 2.1, are two intrinsic donors suggested to be responsible for ZnO being naturally *n*-type [21]. This was challenged by Kohan *et al.* [22] who calculated that in Zn-rich conditions $V_O$, which Van de Walle [10] claims to be a deep donor and thus not a dominating donor, should be more abundant than $Zn_i$ due to lower formation energy. Similarly, in O-rich conditions $V_{Zn}$ should be more abundant than $O_i$ for the same reason. $Zn_i$ is regarded as a shallow donor [23,8], but as Kohan *et al.* have shown, the concentration of $Zn_i$ is not high enough, due to high formation energy, to be responsible for the *n*-type conductivity observed [22]. Experiments and calculations by Look *et al.* [9] indicate that complexes such as $Zn_i$—$N_O$ and $Zn_i$—$Li_{Zn}$ are both shallow donors which may contribute to the *n*-type conductivity.

$V_{Zn}$ and $O_i$ are intrinsic acceptors in ZnO. $V_{Zn}$ has been studied by positron annihilation spectroscopy (PAS) and are the dominating intrinsic acceptors in electron irradiated ZnO [24] and in $O^+$ irradiated ZnO [25]. In the latter it was also shown that $V_{Zn}$ is responsible for compensation and thus high resistivity in $O^+$ irradiated ZnO.

### 2.2.3 Donors

Several extrinsic donors are listed in Table 2.2, and some of them have been suggested to be responsible for *n*-type conductivity in ZnO. $H_i$ or $H_O$ have been suggested by Van de Walle and Janotti [10, 20] to be responsible for the the unintentional *n*-type doping of ZnO. This may well be correct in as-grown samples, but several studies show an out-diffusion of hydrogen at reasonably low temperatures ($\geq$500 °C) [26, 27] without a dramatic conductivity drop, suggesting that either an intrinsic donor or an impurity is still providing electrons after H has diffused out. Al is a donor suggested to be responsible for the unintentional *n*-type doping of ZnO, but it is unlikely that Al is present in every growth method available.

Table 2.2: *Energy levels of selected n-type dopants in ZnO. $E_c$ is the conduction band edge*

| Defect | Energy level ($E_c - E_d$) [meV] |
|---|---|
| Al | 52 [28] |
| In | 63 [28] |
| Ga | 55 [28] |
| H | 46 [28] |

*n*-type doping of ZnO can be achieved with group-III elements like Al, Ga and In substituting for Zn as shown by Minami *et al.* [29].

### 2.2.4 Acceptors

*p*-type doping is difficult to achieve in ZnO as well as some other wide bandgap semiconductors like GaN and ZnSe. Suggested dopants include substitution of Zn by group-I elements like Li, K and Na, or substituting O with group-V elements like N, P, As and Sb. However several problems arise:

1. The dopant has low solubility in ZnO [30].
2. The dopant is a deep energy level acceptor.
3. The dopant is compensated by native defects [31] or background impurities.
4. The dopant is amphoteric, meaning it may act as both donor and acceptor depending on its position in the lattice.

Despite the problems listed above, *p*-type conversion has been achieved with Li [32, 14], As [33, 34], Sb [35, 36], P [37, 38] and N [39, 40, 41, 42]. But problems with reproducibility and stability remain. Arsenic doped *p*-type ZnO has been shown, but not by the expected mechanism. Rather than residing on O-site, there were indications that As atoms resided on Zn-site and acted as a donor, but the size-mismatch induced two zinc vacancies which are acceptors. The total complex As—$2V_{Zn}$ was found to be an acceptor with 150 meV ionization energy [34]. Of the group V elements, N has been considered the most suitable *p*-type dopant in ZnO. This is due to the stability of the dopants on O-site, compared to formation of $AX$ centers*. Nitrogen is calculated to be more stable on O-site, whereas P and As are more stable as $AX$ centers [43]. Table 2.3 lists the reported ionization energies of selected acceptors.

### ZnO doped with lithium

Group I elements substituting for Zn should act as acceptors in ZnO, but *p*-type doping by these elements has appeared to be difficult. $Li_i$ as a donor and $Li_{Zn}$ as an acceptor has been identified by Lander [6], confirming that Li has amphoteric properties in ZnO. Since Li acts amphoteric, it often produces high resistive ZnO. This is the case in hydrothermal (HT) ZnO because LiOH is used in the synthesis resulting in a relatively high Li content in wafers, typically $5 \times 10^{17}$ cm$^{-3}$. The Li content is possible to reduce

*An $AX$ center is a complex of an acceptor and an unknown defect

Table 2.3: *Energy levels of selected p-type dopants in ZnO, collected from Ref. [43] unless otherwise specified.* $E_v$ *is the valence band edge*

| Defect | Energy level ($E_a - E_v$) [meV] |
|---|---|
| N | 400, $165 \pm 40$ [44] |
| P | 930 |
| As | 1150 |
| $Li_{Zn}$ | 90, $110 \pm 10$ [32], $\geq$500 [28] |
| $Na_{Zn}$ | 170 |
| $Li_{Zn}$–$N_O$ | 138 [15], 126 [13], 95 [14] |

by high temperature heat treatment of the wafers, causing out-diffusion of Li [45].

Despite the amphoteric nature of Li, *p*-type ZnO has been reported using Li as the only dopant, and the acceptor activation energy was shown to be $110 \pm 10$ meV [32]. The activation energy is a subject of dispute, and Li has also been shown to be a deeper acceptor ($\geq E_v + 500$ meV) by Meyer *et al.* [28]. The solubility of Li in ZnO is very high, up to 30 % of Zn can be replaced by $Li_{Zn}$ [46], such that $Li_{Zn}$ is an attractive candidate for *p*-type doping.

Another effect of Li that has been observed is clustering of vacancies. Chen *et al.* implanted HT ZnO with Li and characterized the samples with a slow positron beam. After annealing at 500 °C, they observed large vacancy clusters and even micro-voids that annealed out at higher temperatures [47]. Børseth *et al.* observed a similar clustering after 20 ms flash anneals, which also lead to a lowering of resistivity, explained by deactivation of Li acceptors by the vacancy clusters, a feature not seen in conventionally annealed samples [11].

### ZnO doped with nitrogen

Nitrogen has been explored as a *p*-type dopant in ZnO because of its success in ZnSe [48,49]. Nitrogen occupies O sites and is a reasonably shallow acceptor with acceptor level 160-200 meV [50,44]. Unfortunately the solubility of $N_O$ is low ($\sim 3.8 \times 10^{17}\,cm^{-3}$), but can be enhanced by co-doping methods. Komatsu *et al.* observed a 400-fold increase in solubility by co-doping with Ga [51].

Nitrogen concentrations of $10^{19}\,cm^{-3}$ has been achieved without p-type conversion [52]. This may indicate that nitrogen is more readily compensated in ZnO than ZnSe, or that N may occupy sites in which it is not electrically active. Lee *et al.* calculated that N-doped ZnO may be compensated by $(N_2)_O$ combined with $N_O$—$(N_2)_O$ complexes [53]. This has also been confirmed by Li *et al.* in an experiment designed to reveal the compensation source in N-doped ZnO [54].

Stability is also an issue in N doped ZnO. Lu *et al.* showed that N doped *p*-type ZnO reverted to *n*-type ZnO after less than 6-months [14]. A similar behaviour was observed by Xiao *et al.* in N doped *p*-type ZnO, which turned *n*-type after irradiation by 2.72 eV photons, and reverted to *p*-type after a 27 h relaxation time [42].

Chen *et al.* observed an interesting annealing behaviour in $N^+$ implanted HT ZnO characterized by positron annihilation, where results were explained as follows: Implantation induced damages first partially anneals out at 800 °C, then at 1000 °C, thermally generated vacancies form stable complexes together with Nitrogen [55]. Børseth *et al.* observed acceptor activation in Nitrogen implanted HT ZnO at 800 °C, but questions were raised as to whether Li or N were responsible [12].

### ZnO co-doped with lithium and nitrogen

As described above, $Li_i$ is a donor compensating $Li_{Zn}$ in ZnO. And similarly $(N_2)_O$ is compensating $N_O$. Therefore a way to repress $Li_i$ or $(N_2)_O$

formation is of interest. Co-doping Li and N has been tried by Wang *et al.* and stable *p*-type ZnO produced by RF-magnetron sputtering was reported [13]. They reported $Li_{Zn}$–N complexes found by XPS measurements, and estimated an acceptor level at ∼126 meV. Lu *et al.* reported stable *p*-type ZnO:(Li,N) grown by PLD [14]. They compared with ZnO:Li and ZnO:N and found that the co-doped samples were stable after 1 year, whereas the mono-doped samples converted to *n*-type in less than 6 months. They estimated the acceptor energy to be 95 meV. Duan *et al.* later suggested that $Li_{Zn}$–$N_O$ could not be the responsible acceptor due to high formation energy, based on *ab-initio* calculations. They argued that reduction of compensating defects like $Li_i$ by co-doping with N was a more likely mechanism [56]. Recently Zhang *et al.* identified $Li_{Zn}$–$N_O$ as an acceptor with energy level 138 meV and $V_{Zn}$ with an energy level 248 meV [15] in ZnO:(Li,N) produced by PLD. They suggested that both of these may be responsible for *p*-type conduction.

# Chapter 3

# Experimental techniques

This chapter describes the experimental procedure used in this thesis. First the sample preparation and work flow are presented, then a review of the most important characterization techniques is given.

## 3.1 Sample preparation and work flow

In this work commercially available HT ZnO wafers $10\times10\times0.5\,\mathrm{mm}^3$ having a resistivity of $\sim 10^2\,\Omega\cdot\mathrm{cm}$ and a high Li content ($\sim 1\times10^{17}\,\mathrm{Li/cm}^3$) are used as the starting material labeled as High Li sample. Two wafers were pre-annealed at 1000 °C and 1500 °C for 1 hour in air, resulting in a decrease of Li concentration down to $5\times10^{16}$ and $1\times10^{14}\,\mathrm{Li/cm}^3$ and labeled Medium and Low Li, respectively. The complete work flow scheme is illustrated in Figure 3.1. In accordance with the method developed in Ref [45], the 1500 °C pre-anneal was followed by surface polishing before further processing. In short, the polishing was done by mounting the sample in an alumina ring setup and grinding it with 2400 and 4000 grade SiC paper to ensure the flatness of the sample. Then it was polished using 15, 6, 3 and 1 $\mu$m polycrystalline diamond particles on a textile, sequentially. The samples were then implanted with $N^+$ ions using a dose of $\sim 3.5\times10^{15}\,\mathrm{cm}^{-2}$. The High and Low Li samples were implanted us-

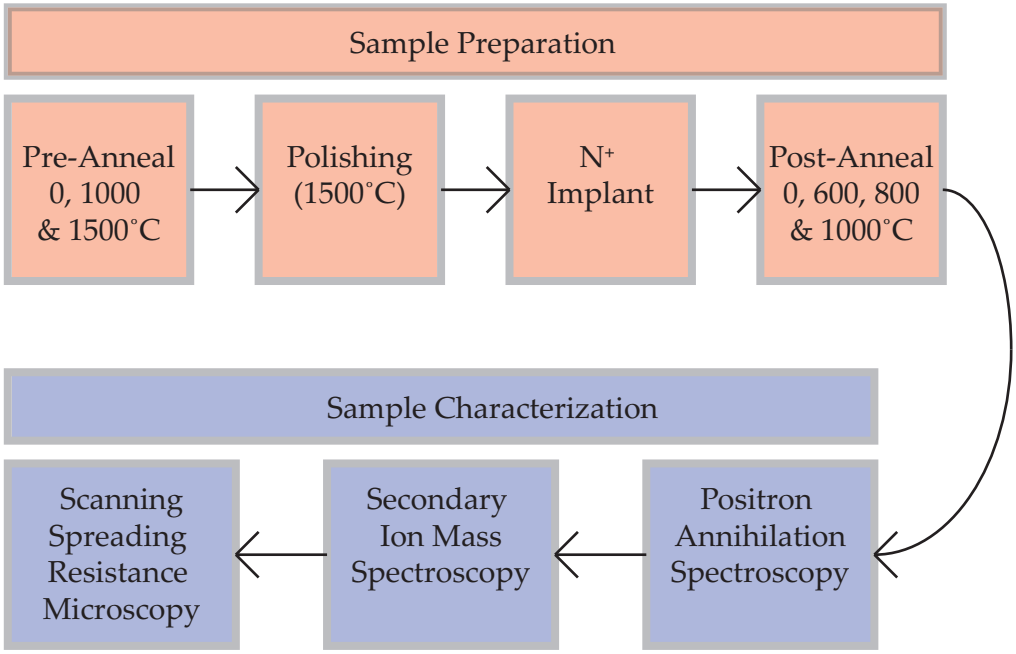


Figure 3.1: *Sample work flow illustrating both sample preparation and characterization*

ing an energy of 500 keV, whereas the Medium Li sample was implanted with an energy of 800 keV. After ion implantation, the wafers were cut into 4 pieces ($5 \times 5\,\mathrm{mm}^2$) and annealed in air for 1 hour, at temperatures 600, 800 and 1000 °C, leaving one un-annealed sample for reference. The annealings were performed in a horizontal tubular furnace using a sample holder made of alumina.

The samples were measured using three different techniques; positron annihilation spectroscopy, secondary ion mass spectrometry and scanning spreading resistance microscopy, in that order. No particular preparation is needed for PAS and SIMS measurements. For SSRM, where a cross section measurement is done, we need to create a flat surface for optimum conditions to perform resistance measurements. In addition we need to ensure good electrical contact between the sample and the instrument base (back contact).

The flat surface is created by simply cleaving the sample. First a dent is

made on the edge of the implanted side, then the samples is put on a piece of cloth, implanted side down. A diamond tipped pen is placed close to the dent made and pressure is applied until the sample breaks. A nice flat cross section surface is often the result.

Good electrical contact is ensured by placing the sample on a piece of copper tape and dabbing a tiny amount of InGa on the sample, then wrapping it up in an easy to handle package with the surface to be measured sticking out.

## 3.2 Positron Annihilation Spectroscopy

Positron Annihilation Spectroscopy (PAS) is a technique to measure concentration and type of defects in metals and semiconductors. Positrons were predicted by Dirac in 1928 and observed for the first time by Anderson in 1932. The positron is the anti-particle of the electron with opposite charge and equal mass to the electron. It is created by the $\beta^+$ decay of $^{22}$Na or other radioactive sources. $^{22}$Na produces positrons with energies ranging from 0 to 540 keV. In addition to the positron, a photon with energy E=1.274 MeV is emitted in 90.4 % of the cases, see Figure 3.2. When

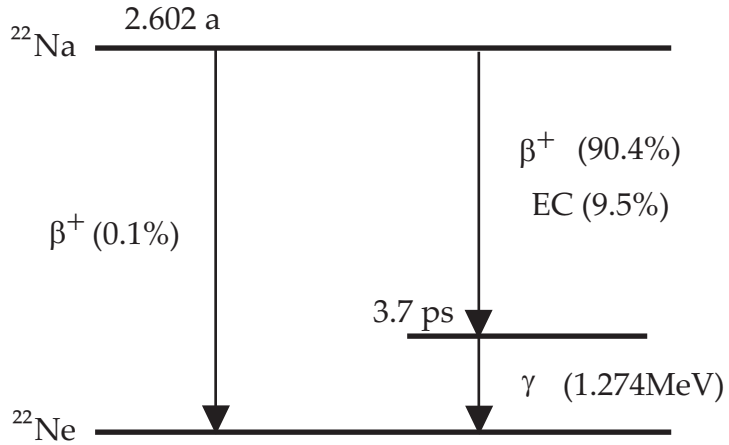


Figure 3.2: *$^{22}$Na radioactive decay scheme. In 90.4 % of decay cases, a photon is emitted immediately after the positron allowing for lifetime measurements. The $^{22}$Na isotope has a half-life of 2.602 years.*

an electron and a positron meet they annihilate and create gamma radiation. There must be two or more photons created by the annihilation due to the conservation of momentum law. It can be shown that annihilation resulting in two photons is the most probable outcome, by a factor of $\sim$370 compared to the second most probable outcome, 3 photons [57]. When a positron enters a crystal lattice it will first thermalize, then diffuse until it annihilates with an electron, see Figure 3.3. If the crystal is perfect the positron will be delocalized and can annihilate with a random electron

in the material after an average lifetime $\tau_{bulk}$. On the other hand, if the crystal contains open volume defects (vacancies or vacancy clusters), the positron is attracted to these due to the lack of a positive nucleus which repulse the positron. Because of the low electron density in such vacancies, the wavefunction of the positrons that enters are changed dramatically, and the positrons become localized. This is called *trapping*, and the vacancies are called positron traps. Because the vacancies have a lower electron

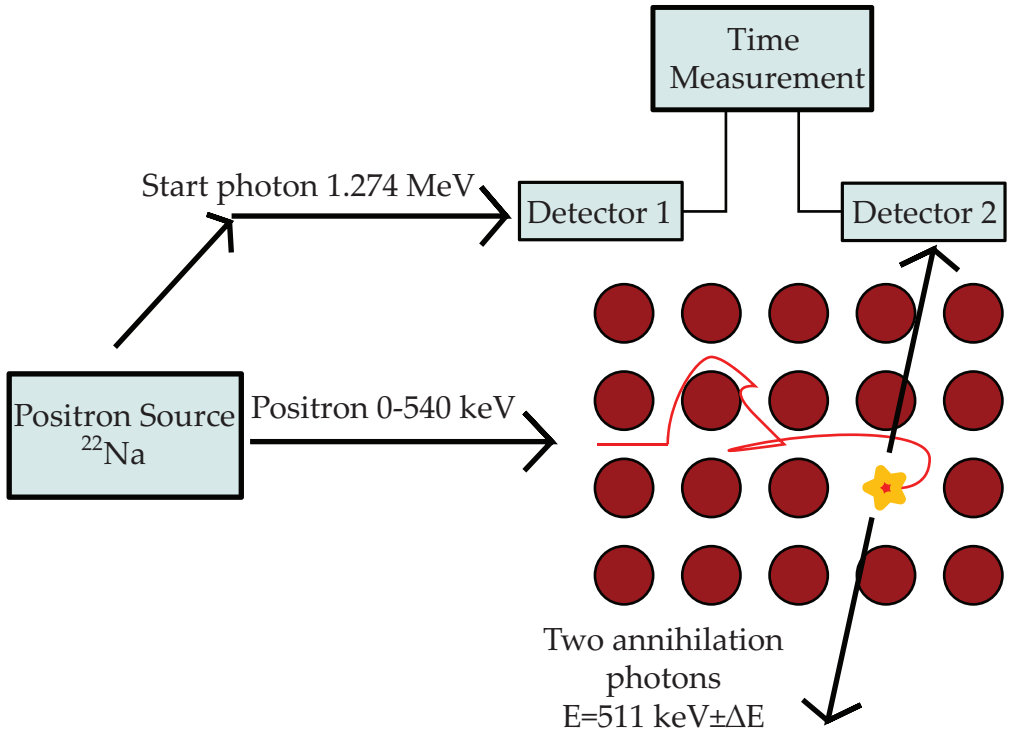


Figure 3.3: *Positron Annihilation Spectroscopy - Basic principles*

density, the lifetime $\tau_V$ of the positron increases accordingly. In addition a positron that annihilate in a vacancy will most probably annihilate with a valence electron of the neighbouring atoms whereas a positron which annihilate in the bulk will have a higher probability of annihilation with a core electron. This affects the annihilation radiation because a core electron have higher momentum than a valence electron. The positron itself has negligible momentum compared to the electrons because it is allowed

to thermalize, whereas the average electron has higher momentum due to the electronic structure of a solid, as explained in section 2.1. This brings us to the two techniques which is most used, Positron Lifetime Spectroscopy and Doppler Broadening Spectroscopy.

### 3.2.1 Lifetime measurements

Positron Lifetime Spectroscopy measures the average lifetime of a positron implanted into the sample. As mentioned, when a positron enters a perfect crystal, it will thermalize, then diffuse in the sample until it annihilates with an electron. This gives the positron an average lifetime in the sample. This lifetime can be measured by first detecting the emitted 1.274 MeV photon from the $^{22}$Na decay, then measuring the time until a 511 keV photon from the annihilation is detected. If the crystal is not perfect, but has vacancy type defects, the positron is attracted to these by Coulomb forces and trapped. Due to the low electron density in the vacancy, the probability of annihilation decreases. Thus the lifetime of the positron increases. Different defects result in different lifetimes, and this makes it possible to extract information about type of defect as well as concentration of defects in a single measurement. This is a major advantage of Positron Lifetime Spectroscopy.

### 3.2.2 Doppler Broadening Spectroscopy

Doppler Broadening Spectroscopy measures the momentum (i.e. the frequency or energy) of the annihilation photons. The positrons are passed through a moderator, often consisting of a single crystalline tungsten foil. The positrons exiting the foil has energies corresponding to the work function of the moderator (typically a few eV), and can be accelerated to a desired energy before being implanted in the sample. This allows for a depth profiling of the surface of the sample. Unfortunately the process of moderating and accelerating the positrons causes loss of correlation between

the 1.274 MeV start photon and the annihilation event, and lifetime measurements are no longer possible.

The mean implantation depth for a positron, $\langle z \rangle$, is related to the energy, $E$, by the following formula:

$$\langle z \rangle = \frac{BE^n}{\rho} \tag{3.1}$$

where the density of ZnO is $\rho = 5,6\,\mathrm{g/cm^3}$. $B = 4\,\mu\mathrm{g/cm^2\,keV^{-n}}$ and $n = 1.6$ are widely used empirical values determined by Vehanen *et al.* [58].

If the electron and the positron were at rest at the instant of annihilation, the emitted photons would have a total energy of 1022 keV corresponding to the rest mass of the positron and the electron, in the two photon annihilation case, 511 keV per photon. But the positron and the electron are not at rest, and so the 511 keV line will broaden:

$$\Delta E = \frac{p_z c}{2} \tag{3.2}$$

Here $p_z$ is the momentum of the annihilating electron—positron pair in the $z$-direction (the line of flight direction of the photons). This results in a distribution change similar to what is illustrated in Figure 3.4. The momentum of the thermalized positron is negligible compared to the electron due to the electron being subject to Fermi statistics, whereas the positron is alone in the crystal. This explains why the broadening is almost only due to the electron momentum. As explained earlier, the positron gets trapped in vacancy type defects. In the vacancy there are mainly valence electrons from the neighbouring atoms. So when the positrons annihilate with low momentum valence electrons in a vacancy, the emitted photons has energies closer to 511 keV. Compare this to positrons annihilating in the bulk where the probability of annihilating with a core electron is higher and thus results in a greater shift in the momentum of the annihilation photons. The S parameter* is defined as the area of the central part of the

**Shape* parameter - Also called the valence annihilation parameter

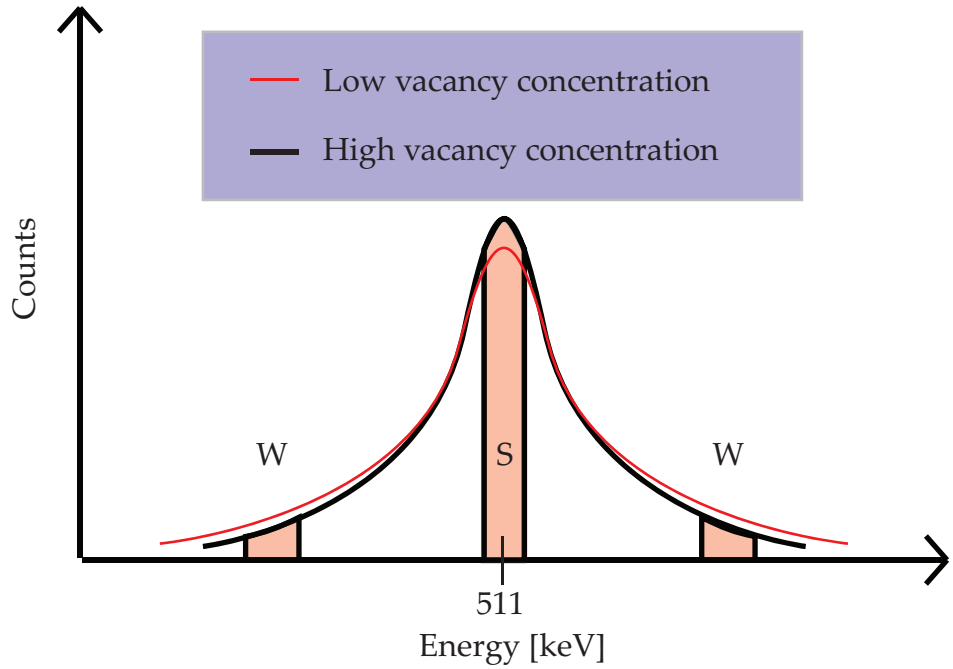


Figure 3.4: *Doppler Broadening - Energy windows of S and W parameters*

annihilation peak, divided by the area below the entire curve, $A_0$,

$$S = \frac{A_s}{A_0}, \quad A_s = \int_{E_0-E_s}^{E_0+E_s} N_D \, dE \tag{3.3}$$

Similarly the W parameter[†] is defined as the high momentum part of the curve divided by $A_0$,

$$W = \frac{A_w}{A_0}, \quad A_w = \int_{E_1}^{E_2} N_D \, dE \tag{3.4}$$

These definitions are illustrated in Figure 3.4. The S and W parameters change according to the concentration and type of defects. Higher concentration of vacancies gives higher S parameter and correspondingly lower W parameter. These data is commonly presented as S(E), W(E) and W(S)

[†] *Wing* parameter - Also called core annihilation parameter

plots. Often all three is presented to give a complete picture. The S(E) plot can in the simplest case (e.g. only mono vacancies present) be read as concentration of defects as a function of positron energy (depth). But if there are other defects present, the S and W parameters are not that simple to interpret. A W(S) plot makes this interpretation easier. It is common to

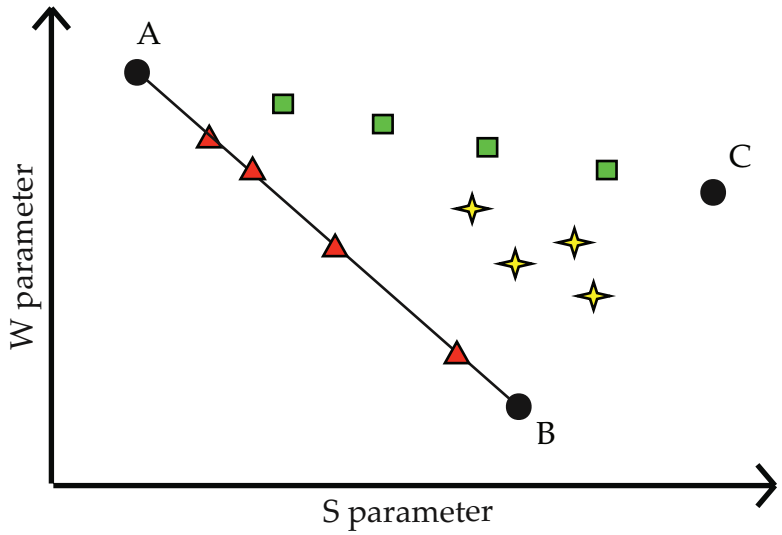


Figure 3.5: *Example of a W(S) plot, where A corresponds to the bulk annihilation state, while B and C are related to the defect states. There are 3 samples shown containing B-type defects (triangles), C-type defects (squares) and a mixture of B and C (stars).*

define two reference points, A and B, corresponding to the bulk values from a defect free sample (A) and values corresponding to a sample saturated with mono vacancies (B). If the values measured deflect from the line between A and B, we know that defects other than mono vacancies are present in the sample. If there are two defects (B and C) that trap positrons, the points in the plot are values determined by the triangle of A, B and C. This is illustrated in Figure 3.5. In depth profiling experiments, it is important to note that the positrons implanted with low energies will diffuse to the surface and annihilate with surface states, which may look like a separate defect. Therefore we often omit the positrons implanted with en-

ergies lower than 4 eV in W(S) plots. To make the data comparable to experiments done in other labs and with other chosen energy windows, it is common to normalize the data using values from a defect free reference sample, $S/S_{ref}$ and $W/W_{ref}$.

Doppler broadening spectroscopy and lifetime measurements can be performed with temperature as a parameter to provide more information about the observed defects. In particular, information about the ionization energy of the defects. This is due to the ionization of defects by means of thermal excitation. Temperature dependent PAS is useful because positrons only get trapped at neutral and negative defects. This means that donor-type defects which is positive at high temperatures and thus invisible to positrons, becomes neutral at temperatures below the ionization energy ($kT < E_d$) and detectable by positrons. The opposite is the case for acceptor-like defects, which may be negative at high temperatures ($kT > E_a$) and thus very attractive for positrons, but neutral at low temperatures so that positrons is less attracted to it. The acceptor/donor nature of a defect can be determined in addition to its ionization energy. A limitation of the method is that at low temperatures (<150 K) the surface of the sample acts as a molecular trap where gas molecules in the vacuum chamber condenses. This may lead to a charged surface which attracts shallow implanted positrons and the condensed gases also provides new annihilation sites. In all, this limits low temperature measurements to bulk samples, as thin film measurement data often becomes corrupted.

## 3.3 Secondary Ion Mass Spectrometry

Secondary Ion Mass Spectrometry (SIMS) is a technique used to characterize the concentration of dopants in semiconductor surfaces and thin films. It is based on the physical phenomenon called sputtering, in which energetic ions bombards a sample and the sample ejects particles. In SIMS, the energetic ions called the primary beam, with energies between 3-15 keV, is focused and directed towards the sample in which ions, atoms and molecules are sputtered off. Only the ions are detectable as they can be controlled by electric and magnetic fields, and they create what we call the secondary beam. The ionized particles are then accelerated and filtered in two stages before hitting a detector. First they move through an electric field and a slit which separates the ions by energy. Then the ions of equal energy passes through a magnetic field and a slit which separates the particles by momentum. The path of primary and secondary ions are illustrated in Figure 3.6. The particles that have passed through both filters have the same mass-to-charge ratio.

$$\frac{M}{q} = \frac{r_m B^2}{r_e E_0} \tag{3.5}$$

If the magnetic field strength is changed we also change the mass-to-charge ratio of the particles that hit the detector as indicated by Equation 3.5. We then measure number of counts as a function of time and magnetic field.

An important quantity in SIMS is the sputtering yield, which is defined as the ratio of emitted secondary atoms to incoming primary ions $Y = N_s/N_p$. Typical yield values is in the range of 1-15. Note that $N_s$ includes neutral atoms and molecules, and that only ionized species are detectable in SIMS. Yield is dependent on the primary ions mass, energy and angle of incidence, in addition to the target atom mass and its surface barrier height for atomic emission. Ionization probability is another important quantity, but no accurate theory exist to describe it. Ionization probability

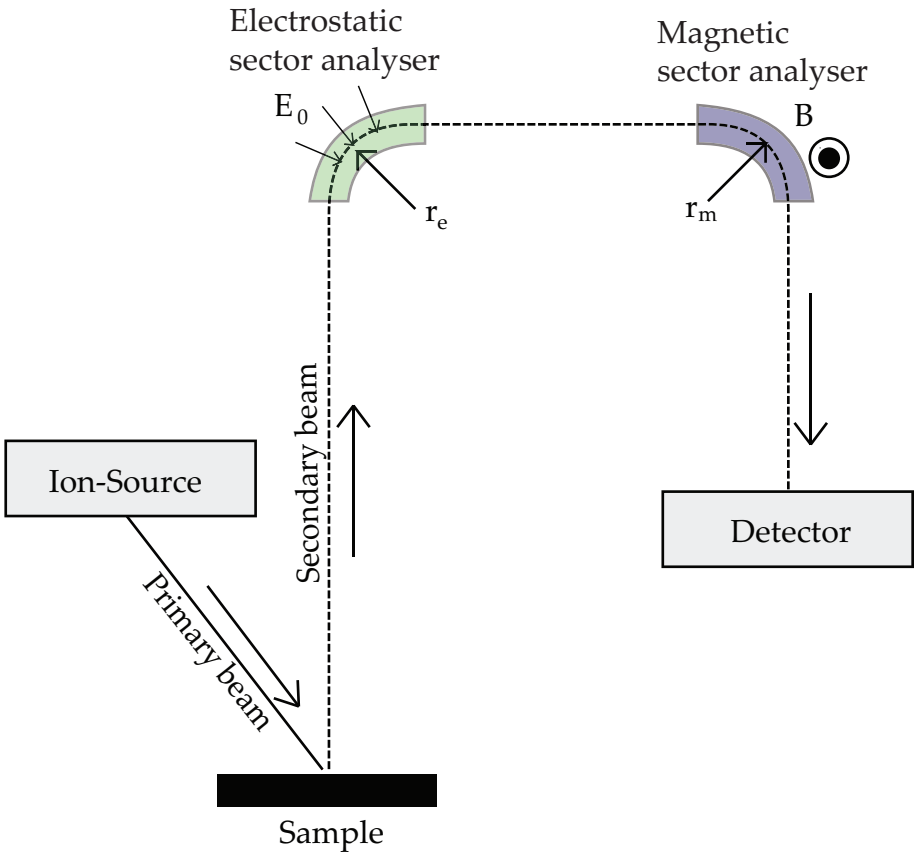


Figure 3.6: *Secondary Ion Mass Spectrometry - Basic principles*

is dependent on ionization energy[‡] and electron affinity[§] of the sputtered species, for positive and negative ionization respectively. This means that elements to the right in the periodic table tends to be negatively ionized and vice versa. The ionization probability can be enhanced by the type of primary ion. An electronegative primary ion promotes positive ionization (left side of periodic table), and an electropositive primary ion promotes negative ionization (right side of the periodic table). For this reason most SIMS setups are equipped with two sources of primary ions, often oxygen

[‡]Ionization energy is the energy required to remove an electron from a gaseous atom or ion.

[§]Electron affinity is the energy change that occurs when an electron is added to a gaseous atom.

($O_2^+$) and cesium ($Cs^+$).

By rastering the beam over a square, a crater is created and the concentration as a function of depth ($z$) can be measured, this technique is called depth profiling. In this mode the counts of each element to be monitored is registered within a certain time window. The number of counts is proportional to the concentration of the element by multiplying with a relative sensitivity factor $RSF$.

$$\frac{I_R}{I_E} = RSF\frac{C_R}{C_E} \tag{3.6}$$

Where $I_R$ is the intensity of the reference species or matrix, and $I_E$ is the intensity of the species of interest. This factor is determined by measuring a reference sample with a known concentration of the dopant in question. A reference sample can be created by ion implanting a sample with a known dose, and then integrating the measured SIMS profile to determine the concentration at the implantation peak. In depth profiling mode SIMS is capable of detecting concentrations smaller than $10^{15}\,\mathrm{cm}^{-3}$, or to put this in perspective; 1 impurity atom out of a billion lattice atoms is detectable, which is truly a magnificent sensitivity.

Other modes of operation is imaging and mass spectrum. In imaging mode a two dimensional image of the rastered plane is generated, and changes in concentration as a function of $x$ and $y$ is visualized. In mass spectrum mode the entire mass-to-charge spectrum is scanned by changing the magnetic field in the magnetic sector analyzer continuously, making it possible to determine which elements are present in the sample. The results are usually plotted as a histogram plot with mass on $x$-axis and counts/s on $y$-axis. A mass spectrum plot can be difficult to interpret as we see only the masses of an ion, which may consist of one or more atoms. This is called mass interference, and is a very common problem in SIMS. An example of this occurs in phosphorous doped silicon, where $^{31}P$ has approximately the same mass as $^{30}Si^{1}H$, $^{29}Si^{1}H_2$ and $^{28}Si^{1}H_3$. $^{30}Si^{1}H$ (30.9815957 amu)is closest to $^{31}P$ (30.9737620 amu) in mass and very high mass resolution is needed to discriminate between these two ($M/\Delta M = 3955$).

In addition quantification is difficult, because each observed element requires calibration using a reference sample. Without the calibration we only observe an intensity [counts/second], and not a concentration.

A common problem that arises is the charging effect. This is caused by highly resistive samples, or a high resistivity layer due to ion implantation, leading to positive charge buildup at the surface. This charge deflects incoming ions and corrupts the measurement. Often this effect can be countered by using an electron gun to compensate by adding negative charge (electrons) to the measured surface.

## 3.4 Scanning Spreading Resistance Microscopy

Scanning Spreading Resistance Microscopy (SSRM) is a mode of Scanning Probe Microscopy (SPM), in which a conductive SPM-tip is put in contact with a sample and scanned across the surface. Another mode is Atomic Force Microscopy (AFM), which is usually conducted in tapping mode, which means that the tip is vibrating from an applied sinusoidal force $F_\omega$ close to its resonance frequency. In tapping mode the tip is only touching the surface intermittently and causes little damage to the surface and tip. A less sophisticated mode is contact mode, where the tip is pressed into the surface by a constant force and thus inflicts more damage to the surface and tip than tapping mode. In both modes the vertical motion of the tip is measured by a laser which is reflected of the cantilever of the tip to a photodetector. SSRM is conducted in contact mode and differs from AFM in that a DC bias is applied to the conducting tip so that a current passes through it and we can measure variations in resistance in addition to topography. This makes it possible to visualize a 2D picture of the resistivity of a surface.

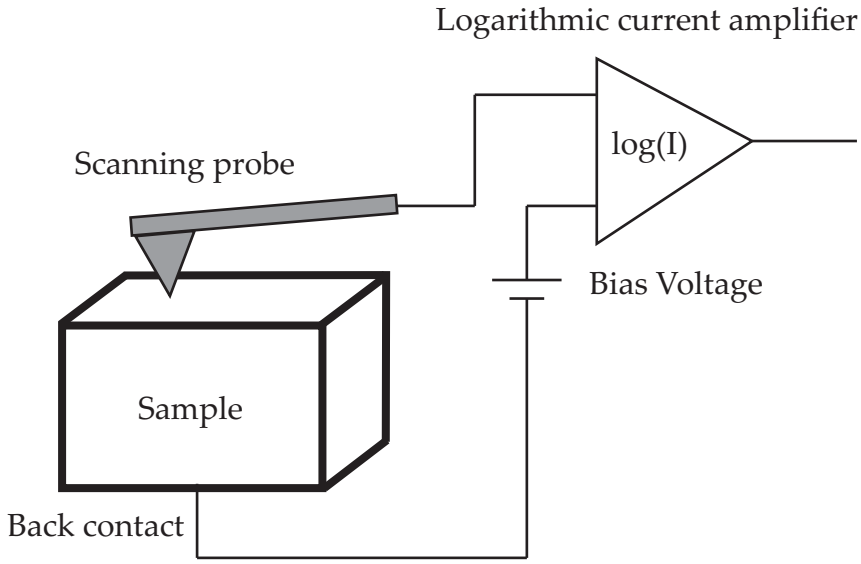


Figure 3.7: *Scanning Spreading Resistance Microscopy - Basic principles*

The resistance measured is a sum of several components, namely spreading resistance $R_s$, contact resistance $R_c$ (between tip and sample as well as back contact), probe resistance $R_p$ and bulk sample resistance $R_{bulk}$:

$$R_{tot} = R_s + R_c + R_p + R_{bulk} \tag{3.7}$$

$$R_s \approx \frac{\rho}{4a} \tag{3.8}$$

Where $a$ is the radius of the tip and $\rho$ is the resistivity. Of these components, only the spreading resistance, $R_s$, varies as we scan across a small area of the sample. The other components should be as low as possible to achieve accurate measurements. The resistivity is the inverse of conductivity $1/\rho = \sigma = qn\mu$ where $n$ is carrier concentration and $\mu$ is the carrier mobility. Extracting carrier concentration is a challenging task since it is dependent on both mobility and tip radius, which may not be known. Tip radius may even change during measurement due to tip wear, and comparison with samples of known resistivity is needed at every measurement to make quantitative measurements. Also damage to the sample due to the pressure of the tip towards the surface is a drawback. Still, a qualitative measurement of carrier concentration across a sample is readily achieved, and it is possible to resolve carrier concentration differences of about 15% [59] within a huge dynamic range ($10^{16}$ to $10^{20}$ $\mathrm{At/cm^3}$ [60]). Another great advantage of SSRM is the precision in spatial resolution (<3 nm) [60]. SSRM can be utilized on a cleaved wafer to measure the cross section so that a depth profile (resistivity vs. depth) can be plotted based on an average of several scanned lines.

# Chapter 4

# Results

In this chapter the experimental results are presented. Three characterization techniques are used; SIMS, PAS and SSRM. The results will then be discussed in Chapter 5 and compared with each other in order to extract information on the mechanisms and defects involved.

## 4.1 N and Li concentration measurements

To obtain the N and Li* depth profiles a Cameca IMS 7F Secondary Ion Mass Spectrometer (SIMS), with $Cs^+$ and $O_2^+$ as the primary beam, respectively, have been employed. As a reference signal the ions $^{70}Zn^{16}O_2^-$ and $^{70}Zn^+$ were chosen with the $Cs^+$ and $O_2^+$ sources, respectively. The SIMS sensitivity for nitrogen and lithium is around $10^{17}\,cm^{-3}$ and $10^{13}\,cm^{-3}$, respectively. The high lithium sensitivity is achieved by increasing primary beam current and reducing raster size, but note that this also results in reduced depth resolution.

The samples as described in Section 3.1 were measured in depth profiling mode to establish the concentration of nitrogen and lithium as a function of depth. The samples are referred to as the High Li, Medium Li and

*Only the $^7$Li isotope is measured and shown in the plots herein. The natural abundance is 92.41 % $^7$Li, and 7.59 % $^6$Li [61].

Table 4.1: *Summary of Li concentration measurements in as-implanted samples.*

| Sample | Li conc. [$cm^{-3}$] |
|---|---|
| High Li | $1 \times 10^{17}$ |
| Medium Li | $5 \times 10^{16}$ |
| Low Li | $3 \times 10^{14}$ |

Low Li samples, according to their bulk Li content as measured by SIMS and summarized in Table 4.1. The plots are shown in Figures 4.1, 4.2 and 4.3, respectively. In addition Figure 4.4 illustrate the Li content to a depth of 27 $\mu$m in the Low Li samples.

The nitrogen implantation energy was 500 keV in the High and Low Li samples, and 800 keV in the Medium Li samples. This corresponds to a peak at 660 nm and 900 nm, respectively, according to TRIM calculations [62]. As illustrated in Figure 4.1, 4.2 and 4.3, the SIMS profiles shows a nitrogen peak at the same positions as predicted by the TRIM calculations. The long tail of the nitrogen profiles is due to ion channeling during implantation, and is more pronounced at higher implantation energy, even though the critical angle of admitting an ion into a channel is lowered with increasing energy [63]. There are some variations in peak concentration of the as-implanted samples compared with the annealed ones in both the High and Medium Li samples, as can be seen from Figure 4.1 and 4.2. Several measurements were done, and slight differences in concentration were detected in different positions on the same sample. This means it is probably not diffusion related since it is not related to annealing temperature. The reason for this non-uniformity is probably due to fluctuations in the ion beam current. The importance of this for the PAS measurements is small because of the large difference in inspected area during SIMS and PAS measurements. Indeed the PAS equipment used in the measurements described in Section 4.2 has a positron beam with

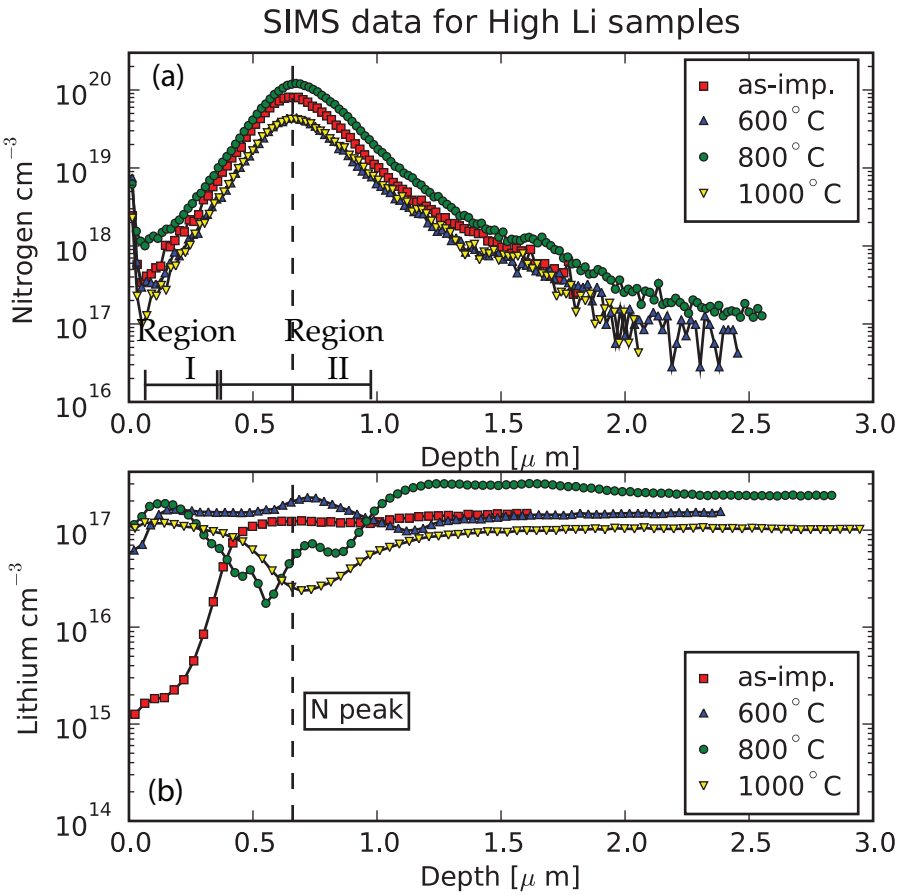


Figure 4.1: *N (a) and Li (b) concentration versus depth profiles in samples containing **High Li** concentration as measured by SIMS*

diameter of 2-3 mm compared to a SIMS crater of $200 \times 200\,\mu m^2$, providing that minor local non-uniformity in nitrogen concentration averages in PAS measurements.

Two regions are defined in the samples for later reference, and are illustrated in Figures 4.1, 4.2 and 4.3. The first is Region I corresponding to the region close to the surface with low N concentration but high implantation induced damage. The other is Region II corresponding to the region close to the peak of N concentration.

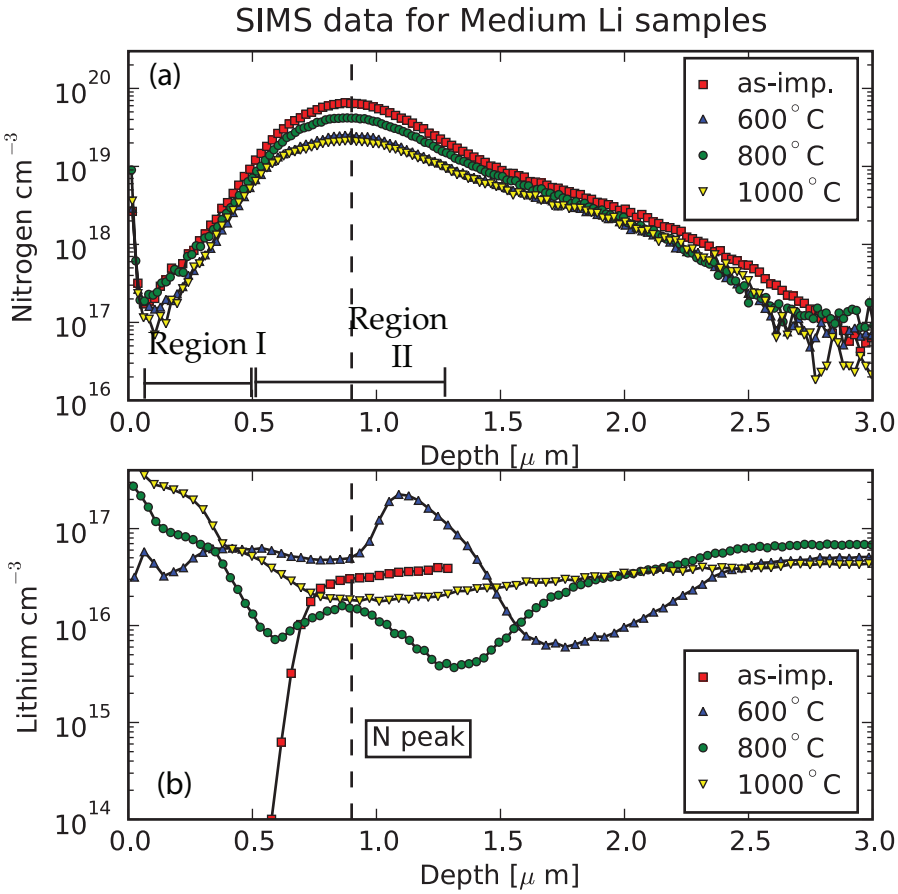


Figure 4.2: *N (a) and Li (b) concentration versus depth profiles in samples containing **Medium Li** concentration as measured by SIMS*

The lithium profiles as plotted in Figures 4.1, 4.2 and 4.3 show a redistribution of Li after annealing at temperatures ranging from 600 to 1000 °C. In the as-implanted samples the Li concentration, as listed in Table 4.1, was constant with respect to depth. Due to charging effects, as described in Section 3.3, the data near the surface was lowered significantly.

In all samples annealed at 600 °C, an agglomeration of Li can be seen slightly deeper than the N peak. Behind this agglomeration region, we see a lowering of the Li concentration before it approaches the original bulk

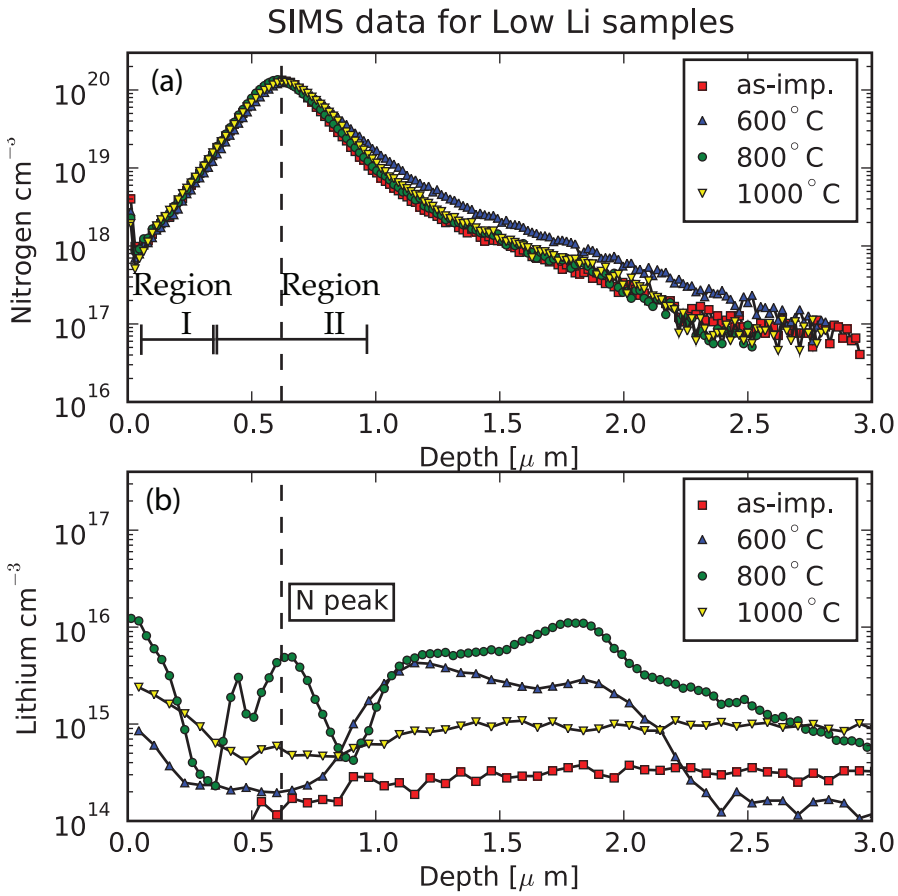


Figure 4.3: *N (a) and Li (b) concentration versus depth profiles in samples containing **Low Li** concentration as measured by SIMS*

level. This characteristic behaviour can be seen in all samples annealed at 600 °C, though it is more pronounced in the Medium Li sample in Figure 4.2. Note that the peak Li concentration is $\sim 2.2 \times 10^{17}$ in both High and Medium Li samples, despite the difference in bulk concentration. In the low Li sample, the Li concentration levels out approximately 4 $\mu$m deep at a level slightly below bulk level, as confirmed in Figure 4.4.

800 °C anneal leads to a maximum in Li concentration at the nitrogen peak in all samples. Also there are two local minima before and after the

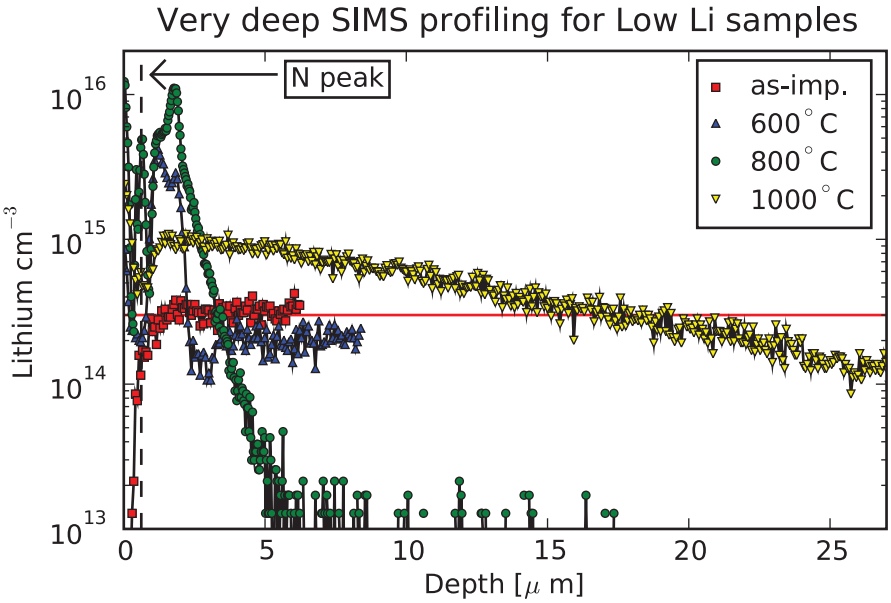


Figure 4.4: *Li concentration versus depth profiles in samples containing* ***Low Li*** *concentration as measured by SIMS. Primary current is increased and raster size decreased to achieve higher sensitivity and sputter rate. The red line is an extrapolation of the as-implanted bulk Li level.*

nitrogen peak, indicating that Li atoms are diffusing from both sides toward the peak and are trapped within the peak. This behaviour is increasingly clear as Li content decreases. In Figure 4.4 we can see that the Li content deeper than 5 $\mu$m is below the Li detection limit of $\sim 10^{13}$.

After annealing at 1000 °C, a minimum Li concentration is observed at the nitrogen peak in all samples. In the High and Medium Li samples, as seen in Figures 4.1 and 4.2, the Li concentration rises back to bulk level at 1.5 and 2.5 $\mu$m, respectively. Figure 4.4 illustrates that this changes dramatically in the Low Li sample, where a slowly decreasing Li concentration gradient goes deep into the sample, and not falling below bulk values before 17 $\mu$m into the sample.

## 4.2 Vacancy depth profiling

The samples prepared were measured at the Technical University of Helsinki using Positron Annihilation Spectroscopy (PAS) to study acceptor type vacancies. PAS was employed in a Doppler Broadening Spectroscopy mode, providing information about neutral and negative vacancies (depth distribution, structure etc.). Slow positrons of energy 0.5-38 keV were implanted in the samples and the annihilation radiation were detected by two Ge detectors which has a resolution of 1.24 keV at 511 keV. The counts at different energy were then processed into the S and W parameters, as described in Section 3.2, where S is the counts in the central part of the annihilation line, $|E_\gamma - 511\,\text{keV}| \leq 0.8\,\text{keV}$. Similarly the W parameter is the counts in the wing of the annihilation line, $2.9\,\text{keV} \leq |E_\gamma - 511\,\text{keV}| \leq 7.4\,\text{keV}$. These energy windows are illustrated in Figure 3.4. Furthermore the S and W parameter were normalized, also described in Section 3.2. Figures 4.5, 4.6 and 4.7 illustrates the PAS Doppler broadening measurements performed on HT samples having High, Medium and Low Li concentration, respectively. Two different plots are made from the data collected, namely S parameter versus Energy plots *S(E)* and W parameter versus S parameter *W(S)* as described in Section 3.2.2. The dashed line in the W(S) plots has the same position and slope in all plots and the slope represents the size of the vacancy clusters (3 to 4 $V_{Zn}$) as observed by Børseth *et al.* [12].

For positron implantation energies corresponding to Region I, as described in Section 4.1, Figures 4.5, 4.6 and 4.7 show that the S parameter increases in the as-implanted sample, having a peak just before the actual N implantation peak which is indicated by the vertical dashed line. The W(S) plots all show a similar behaviour, with points residing on a line deviating slightly from the bulk-$V_{Zn}$ line, indicating that small vacancy clusters, $(V_{Zn})_2$, are created during $N^+$ implantation. It is worth noticing that in Figure 4.7, the S parameter is significantly higher than that in the other samples.

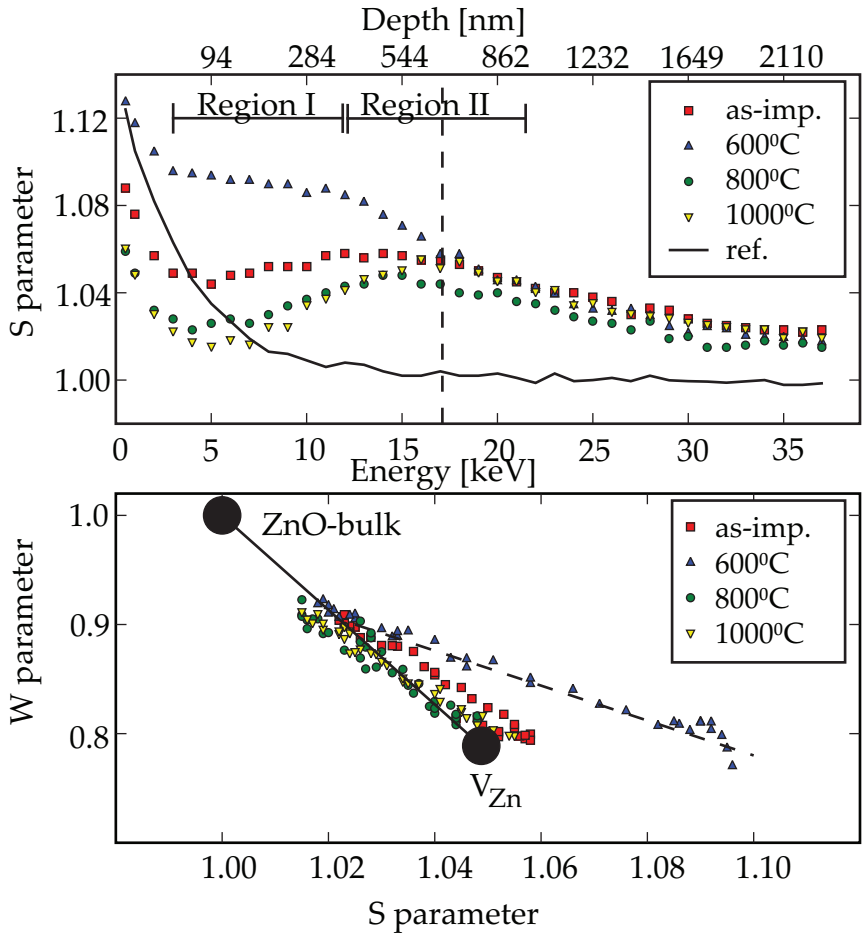


Figure 4.5: *Positron annihilation spectroscopy results for the sample containing* ***High Li*** *concentration. Top: S parameter vs Energy. Bottom: W parameter vs S parameter*

After annealing at 600 °C the S parameter in Region I increase substantially for all samples, see Figure 4.5–4.7. This does not mean that the concentration of vacancies increase, but rather that the nature of the vacancies change. This can also be seen in the W(S) plots, in which the points clearly shows a deviation from the bulk-$V_{Zn}$ line, indicating that large vacancy clusters (3-4 $V_{Zn}$) are present. In addition it can be seen that these points follow the straight dashed line, indicating that the concentration of mono vacancies is constant as a function of depth, and that the concentration of

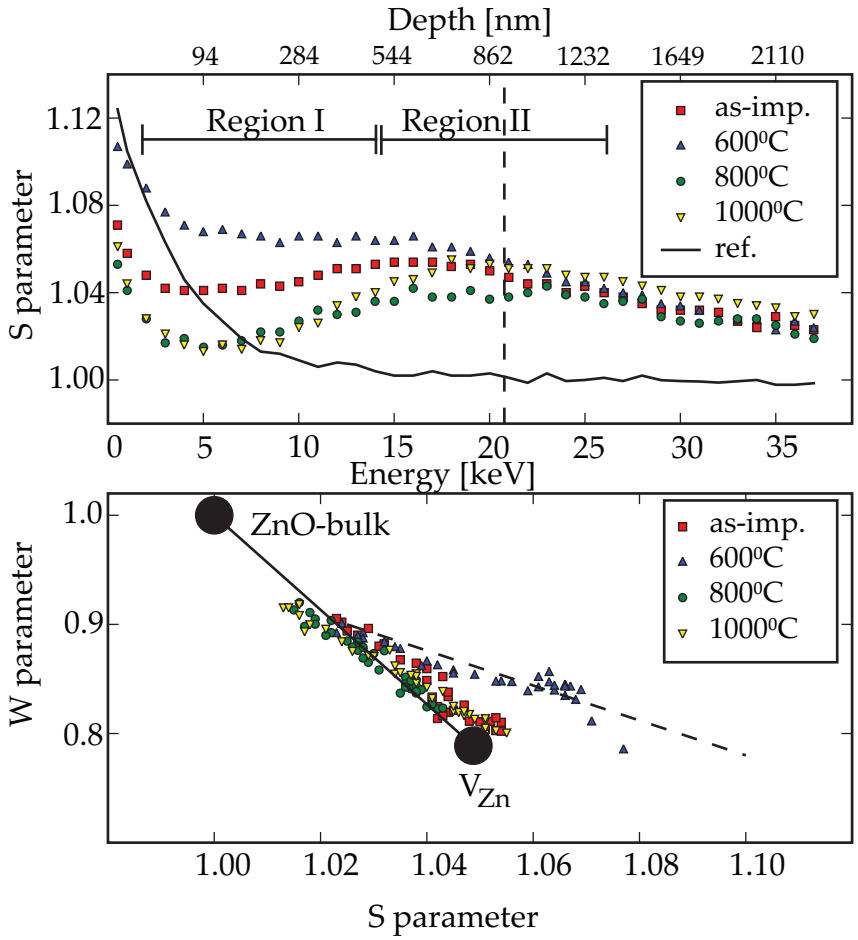


Figure 4.6: *Positron annihilation spectroscopy results for the sample containing* ***Medium Li*** *concentration. Top: S parameter vs Energy. Bottom: W parameter vs S parameter*

the vacancy clusters is varying as a function of depth.

When the samples are annealed at 800 °C, the S parameter in Region I is lowered substantially in the High and Medium Li samples (Figures 4.5 and 4.6), indicating that vacancy clusters dissociate and anneal out, in accordance with previously observed behaviour [55, 12]. Also the W(S) plots in Figures 4.5 and 4.6 show that the points follow a line at a slightly different angle than the bulk-$V_{Zn}$ line. However, the Low Li samples as shown in Figure 4.7 has a very high S parameter in Region I after 800 °C

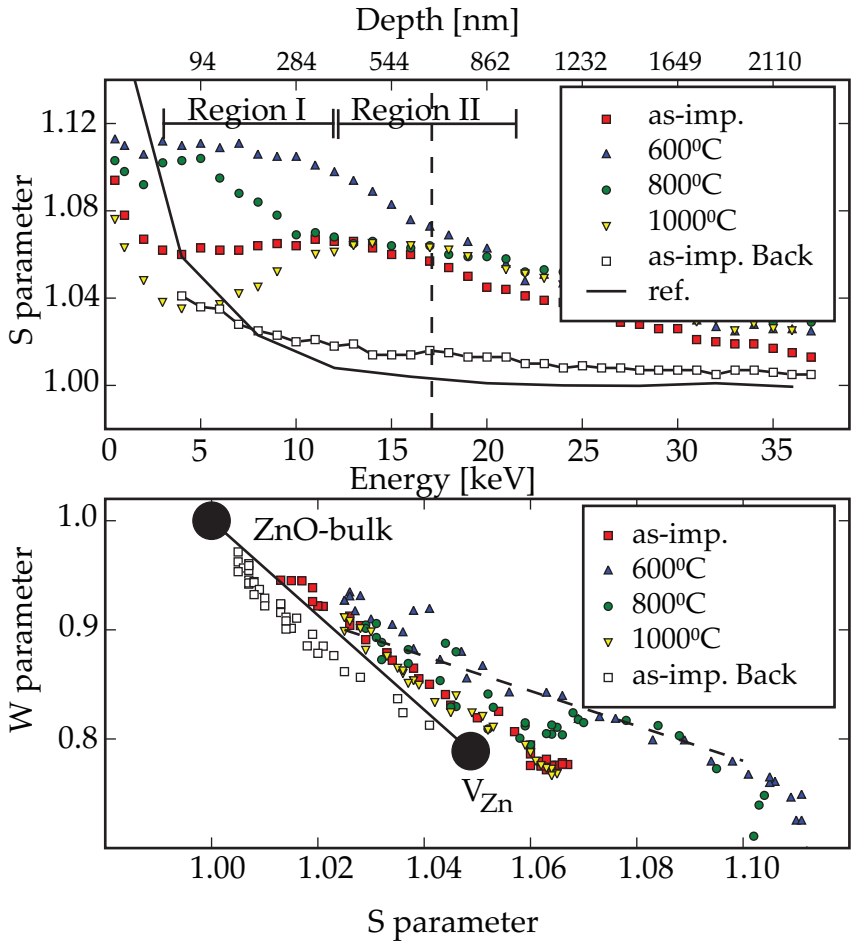


Figure 4.7: *Positron annihilation spectroscopy results for the sample containing* ***Low Li*** *concentration. Top: S parameter vs Energy. Bottom: W parameter vs S parameter*

anneal, contrary to the other samples annealed at 800 °C. In addition the W(S) plot show that large open volume defects still exist.

The 1000 °C anneal leads to further reduction in S parameter in Region I of the High Li sample closer to a typical HT ZnO bulk S parameter value of 1.005[†], indicating that excess vacancies anneal out. In the High and Medium Li samples, only small changes results from the 1000 °C an-

[†]As seen the in back side measurement of the as-implanted Low Li sample in Figure 4.7

neal, because even at 800 °C, most zinc vacancies are annealed out. For the Low Li sample, the S parameter is lowered considerably, but still far from the typical HT bulk value, indicating that vacancy related defects are still present in the sample.

In Region II in Figures 4.5, 4.6 and 4.7, an S parameter maximum is observed slightly before the nitrogen peak in the as-implanted samples. This is as expected after ion implantation, which creates vacancies before the projected range, and self-interstitials at and after the projected range [64]. In accordance with this an S parameter drop is observed after the N peak.

In the High and Medium Li samples, annealing at 600 °C causes an increase in S parameter, compared with the as-implanted samples, which reaches partially into Region II, as shown in Figures 4.5, 4.6 and 4.7. It must be stressed that the implantation depth distribution of positrons is roughly a Gaussian curve which widens with higher implantation energy. This means that the information at any given point includes information from surrounding points, and as such the high S parameter from Region I will have influence on the S parameter in parts of Region II. This may indicate that large vacancy clusters are not present deeper than the nitrogen peak.

Annealing at 800 °C causes a characteristic drop in the S parameter in Region II for the samples containing High or Medium Li. This drop is not observed in the samples annealed at 600 or 1000 °C, nor is it observed in the Low Li sample.

Only small differences in S parameter is observed in Region II after 1000 °C anneal, compared with the other temperatures. The exception is the 800 °C anneal as explained above.

## 4.3 Depth profiling of electrical resistance

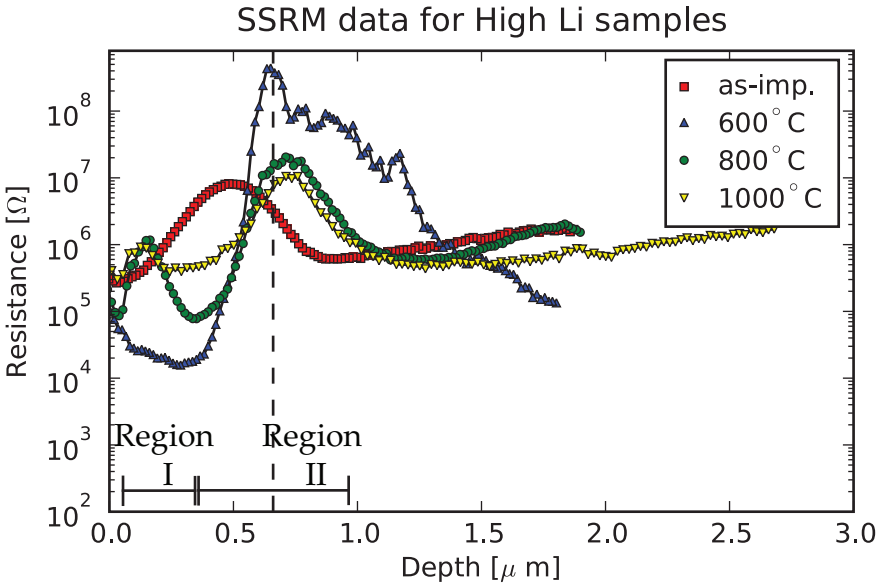


Figure 4.8: *SSRM resistance as a function of depth for* ***High Li*** *samples.*

The samples were prepared for SSRM as described in Section 3.1 and mounted on the sample stage of a Nanoscope Dimension 3100 Scanning Probe Microscope (SPM) from Veeco Instruments. The instrument was equipped with commercial Ti-Pt coated Si tips from $\mu$Mash, with tip radius of curvature $\leq 35\,\text{nm}$.

Figure 4.8, 4.9 and 4.10 shows the spreading resistance as a function of depth in High Medium and Low Li samples, respectively. Note that the absolute resistance is not comparable between measurements. Only changes within one measurement should be compared, due to tip wear, which affects the area measured, and thus the measured resistance as seen in Equation 3.8.

In the as-implanted samples, a resistance peak is clearly seen $\sim 100\,\text{nm}$ before the actual nitrogen implantation peak, as indicated by the vertical dotted line. After the peak, a resistance minimum is seen. In the Low Li sample another peak can be seen at about $2.0\,\mu$m depth before a sharp drop.

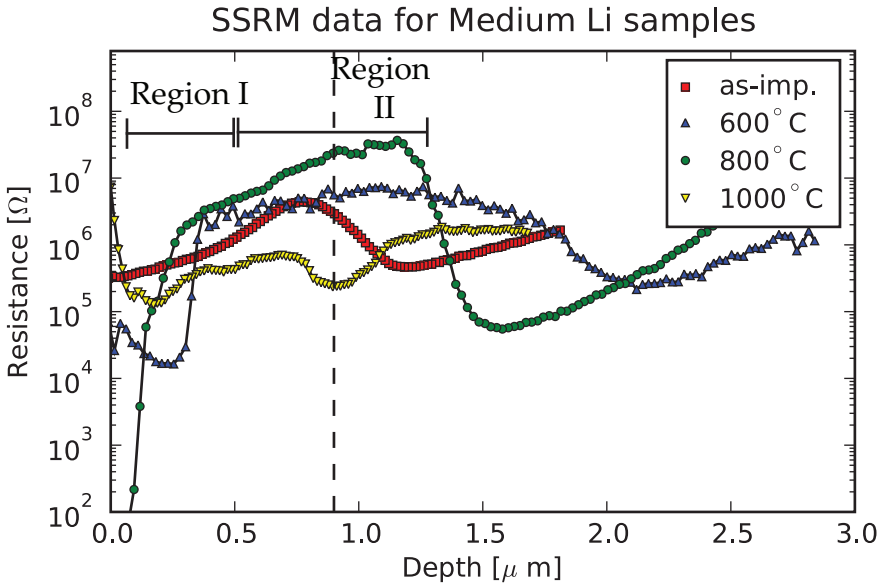


Figure 4.9: *SSRM resistance as a function of depth for* ***Medium Li*** *samples.*

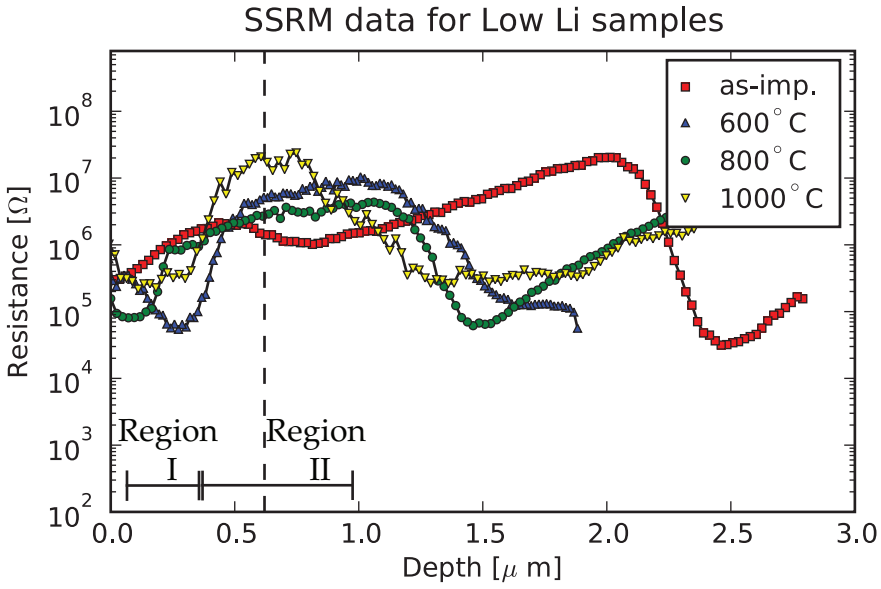


Figure 4.10: *SSRM resistance as a function of depth for* ***Low Li*** *samples.*

After annealing at 600 °C a drop in resistivity is observed in Region I of all samples, compared with the as-implanted samples. In contrast, a significant increase in resistivity is observed in Region II in the 600 °C an-

nealed samples, compared with the as-implanted samples. This behaviour is present in High, Medium and Low Li samples, with resistance difference of approximately 5, 2 and 2 orders of magnitude, respectively. In addition the high resistive region is much wider in the Medium Li sample, correlating to a wider nitrogen implantation peak as seen from Figure 4.2.

Annealing at 800 °C results in rather similar resistance profiles as that at 600 °C, with an exception that there is a second resistance peak very close to the surface. Also the resistance difference between minimum and maximum is 2, 5 and 1 orders of magnitude in the High, Medium and Low Li samples, respectively.

The samples annealed at 1000 °C has $\sim$ 2 orders of magnitude peak-to-peak resistance difference in the High and Low Li sample. The measurement on the Medium Li sample shows a resistance drop in Region II, which is not consistent with the measurements of the High and Low Li samples.

# Chapter 5

# Discussion

In this chapter, the results presented in the previous chapter will be discussed. The experiment was designed to reveal the importance of Li in the mechanism of vacancy clustering and to determine whether Li played a part in the acceptor activation observed by Børseth *et al.* [12]. Li concentration was intended to be the only variable in the experiment. Unfortunately, one error was detected in the Medium Li sample regarding the $N^+$ implantation energy which was higher than intended. In addition an unexpected high concentration of defects as a result of the surface polishing procedure was discovered. In particular the role of Li in vacancy cluster formation (Section 5.2) becomes more complicated to interpret.

## 5.1 Distribution of $V_{Zn}$ and $Zn_i$ in as-implanted samples

First let us look at the as-implanted samples. The SSRM results in Figures 4.8–4.10 indicate a peak in the resistivity about 100 nm from the N peak towards the surface in all as-implanted samples. The PAS results similarly indicate a peak in S parameter at approximately the same position in Figures 4.5–4.7, indicating that the positrons annihilate in zinc vacancies. This is a clear indication that zinc vacancies are the dominant acceptors

responsible for compensation of donors in the region between the surface and the implantation peak. This is in agreement with that shown by Zubiaga *et al.* in $O^+$ irradiated ZnO [25]. In addition, following a sharp decrease in resistivity after the N peak, we observe a resistivity minimum. Due to the momentum of the incoming ions during implantation, and the creation of vacancies in the region before the N peak, we expect higher concentration of interstitials in the region after the N peak. A similar separation between vacancy and interstitial profiles has been studied by Brown *et al.* and found to be correct in ion-implanted Si [64]. In our samples the S parameter also decreases in the end-of-range implantation region indicating lower $V_{Zn}$ concentration (note that PAS gives no information on concentration of interstitials). Still, assuming the damage separation occurs, the resistivity minimum can be explained by an increase of interstitial donors, and the obvious candidates are $Zn_i$ and $Li_i$. Due to the number of Zn atoms being approximately 5 orders of magnitude higher than Li, an assumption that $Zn_i$ dominates is reasonable. In addition Look *et al.* observed a donor as a result of electron irradiation which was identified as $Zn_i$ with a donor level of 30 meV [8]. On the other hand, computational studies has shown that $Zn_i$ has high formation energy and low migration barrier, rendering $Zn_i$ unstable [20], and thus suggesting that it may disintegrate and leave $Li_i$ to dominate as an interstitial donor.

## 5.2 Vacancy cluster formation promoted by Li at 600 °C

In Region I in the High and Medium Li samples annealed at 600 °C, the Figures 4.5 and 4.6 show that the S parameter increases significantly in both samples, but more so in the sample containing more Li. The W(S) plot show a clear deviation from the ZnO bulk-$V_{Zn}$ line indicating that the positrons are annihilating in large vacancy clusters. A similar effect has been observed by Børseth *et al.*, who estimated that the slope indic-

ates that at least 3 to 4 $V_{Zn}$ and probably a similar number of $V_O$ forms vacancy clusters [11]. Importantly the amount of vacancy clusters generated during 600 °C annealing is significantly higher in the High Li sample as compared to that in the Medium Li sample, suggesting a correlation between Li concentration and vacancy clustering*. Note that the comparison between High and Medium Li samples holds despite the aforementioned difference in implantation energy in the samples. This is because the increase in energy leads mainly to a displacement of the damage peak while the concentration of implantation induced vacancies exhibit only minor changes according to TRIM calculations as shown in Appendix A. In other words, if Li concentration would have no effect, the S parameter magnitude in the samples after 600 °C anneal in Figures 4.5 and 4.6 might reach similar values, which is obviously not the case, concluding Li-assisted vacancy clustering in ion-implanted ZnO.

The Li enhanced clustering may be due to Li stabilizing vacancy clusters by forming a Li-$V_{Zn}$ complex. This complex has reduced mobility and allows clusterization with mobile $V_{Zn}$ and $V_O$. Indeed positively charged $V_O^+$ and $Li^+$ are needed to proceed with vacancy clustering, since they are compensating negative charge from $V_{Zn}^-$ and stabilizing the clusters. This explanation is alternative to a mechanism proposed by Chen *et al.* in which $Li_i$ reacts with $O_i$ and forms $Li_2O$, thereby reducing the concentration of $O_i$ available to recombine with $V_O$ and indirectly causing increased clustering of $V_O$ and $V_{Zn}$ [47].

In addition we see from SSRM measurements in Figures 4.8-4.10 that the high resistivity layer in Region I in the as-implanted samples, is converted to a low resistivity layer after the 600 °C anneal. This indicates that simultaneously with the clustering, a compensating acceptor disappears in this region, and $V_{Zn}$ is an obvious cause. This indicates that either (i) the vacancy clusters are electrically inactive, (ii) that a large proportion of the

*Note that the same is not seen in the Low Li samples, which is explained in section 5.5 by polishing induced damage corrupting the measurement data.

zinc vacancies are annealing out simultaneously or (iii) that the clusters are deactivating compensating Li.

## 5.3 Activation of N related acceptors at 600 and 800 °C

A significant increase in resistivity is observed in all samples after annealing at 600 °C in Region II. Note that this high resistivity region coincides with nitrogen enriched regions in the samples, indicating N-related acceptor activation. However, we do not see any reasonable changes in S-parameter profiles in Region II when comparing as implanted and 600 °C annealed samples. This needs an explanation because the presence of negatively charged acceptors should potentially affect positron annihilation results. This is because a positron trapped by an acceptor at lattice position will be localized around the acceptor in a hydrogen-like Rydberg state, causing it to annihilate with random electrons in the lattice, pulling the S and W parameters toward bulk values, as observed by Børseth *et al.* [12]. Let us consider 800 and 1000 °C PAS results first and suggest an explanation later.

Annealing at 800 °C results in a decrease in the S parameter in the vicinity of the N peak, while 1000 °C anneal brings the S-parameter profile in Region II practically back to the original as-implanted value. A possible reason for that may be a constant concentration of $V_{Zn}$ related positron annihilation states in Region II, while the characteristic decrease of the S-parameter is due to nitrogen related acceptor activation. Why do we not observe this drop in S-parameter in the 600 °C samples then? This brings us back to the promised explanation of the relationship between PAS and SSRM profiles after 600 °C anneal.

One scenario can be that 600 °C and 800 °C anneal results in acceptors exhibiting different nature and/or charge states. Acceptors listed in Table 5.1 are suggested based on comparison of the host of experimental data.

Note that complex resistivity variations are observed at all annealing tem-

Table 5.1: *Possible acceptors causing high resistivity in Region II of all annealed samples and S-parameter drop in samples annealed at 800 °C.*

| 600 °C | 800 °C |
|---|---|
| $N_O$ | $Li_{Zn}$–$N_O$ |
| $N_O$–$V_{Zn}$ | |

peratures, suggesting interaction between donors and acceptors having different nature, but only after 800 °C do we observe the lowering of the S parameter at the N peak in the High and Medium Li sample. This may suggest that Li and N forms a complex and since both of them can act as acceptors, the complex may be a double acceptor. In *n*-type ZnO double acceptors have double negative charges and are particularly attractive for positrons, thus this may be the cause of the lowering of the S parameter toward bulk value. It should be noted that the reason we do not observe a lowering of S parameter in the Low Li sample may be due to the polishing induced defects described in Section 5.5.

The most obvious complex involving both Li and N is $Li_{Zn}$–$N_O$ and may be the complex observed here. This is in accordance with recent experiments in which Li and N co-doping has been explored and an acceptor identified as $Li_{Zn}$–$N_O$ is found that is more shallow than N or Li by themselves [13, 14, 15].

As shown by the results herein, Li is highly mobile and very important for electrical properties, and must be considered if present. Look *et al.* claims to have made *p*-type ZnO by N doping of a thin film on vapor phase ZnO substrate [50]. They diffused in Li to make the substrate semi-insulating, so that Hall measurements could be performed without interference from the substrate. The thin film was deposited by Molecular Beam Epitaxy (MBE), using Zn, $O_2$ and $N_2$ as sources. The substrate tem-

perature was 525 °C, which is high enough for Li to diffuse. This means that also the thin film may contain a very high concentration of lithium. Considering the discussion above, the film may even have higher concentration of Li than the bulk if the film has more as-grown defects than the bulk. This in turn may have an effect on the electrical properties of the film, maybe due to $Li_{Zn}$ acceptors or a Li and N related acceptor complex. A SIMS analysis of the Li content of the films might have shed more light on this issue. In addition Yuan *et al.* have recently shown that Li is attracted to the surface of the growing film during MBE growth, where it acts as a surfactant and causes improved film quality [65]. This further supports the notion that the film grown by Look *et al.* in Ref. [50] probably has high Li content.

## 5.4 Accumulation of Li in the implantation region

One selected SIMS result from Figure 4.2 is re-drawn in Figure 5.1 and illustrate the Medium Li sample annealed at 600 °C, and we observe an accumulation of Li slightly after the N peak. This may indicate that defects created during ion-implantation acts as a trap for Li. To see if this hypothesis is correct, a diffusion simulation based on the framework developed by Johansen *et al.* [66] was performed (the matlab code can be found in Appendix B). The simulation was performed with a trap profile as shown in Figure 5.1, and we see that only the right flank of the trap profile is filled with Li diffusing in from the bulk. This means that the Li already present within the trap profile stays there, and mobile Li from the bulk is diffusing into the traps and starts filling the trap profile. If the annealing time was longer, we would expect to see the entire trap profile being filled with Li. The trapping causes a lowering in the Li concentration slightly deeper than the trap profile. Note that the bump in the simulated profile is not as deep as the real one. The reason for this is not known, but it may suggest

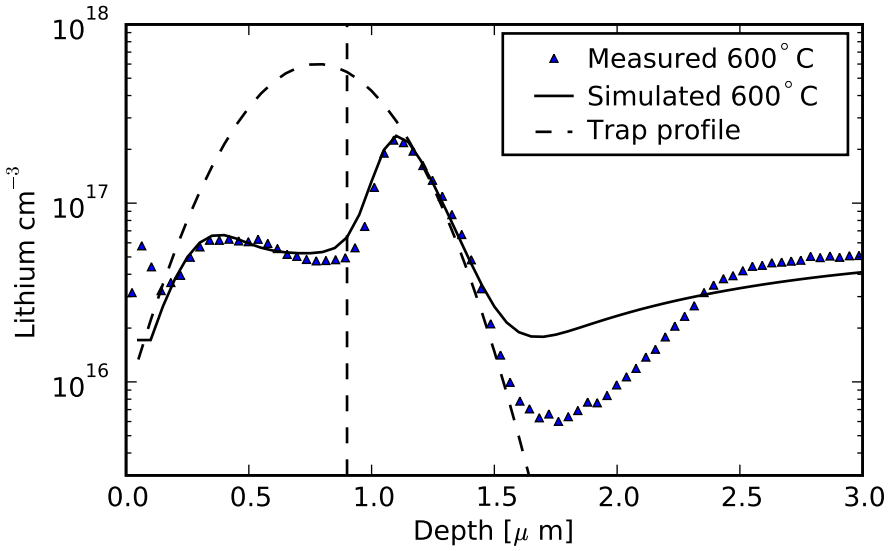


Figure 5.1: *Simulated and measured profiles of Li concentration in* ***Medium Li*** *sample annealed at 600 °C. In the simulation a hypothetical Gaussian distribution trap profile as shown in the figure was used.*

that in addition to the trapping observed, another defect is increasing the diffusivity of Li in this region. One scenario may be that zinc interstitials created during ion-implantation and located slightly deeper than the peak (as argued in Section 5.1), are enhancing the diffusion properties of lithium and thus causing the deep bump.

## 5.5 Annealing behaviour of polishing induced defects

Manufacturing of the Low Li samples involved annealing at 1500 °C and then polishing as described in Section 3.1. Figure 4.7 shows the PAS results from these samples, which differs significantly from the High and Medium Li samples. Starting with the as-implanted sample, the S parameter is high throughout the sample, indicating higher concentrations of

open volume defects, as a result of (i) the high temperature annealing or (ii) the polishing. If (i) where the case, we would expect to see similarly high S parameter on the unpolished backside of the sample, but this is not the case as seen in Figure 4.7. This means (ii) is more likely. In addition the annealing behaviour of the defects observed in the polished sample is very different from the others. In Region I, the 600 °C anneal causes the S parameter to increase to a level higher than in the other samples, whereas a lower S parameter was expected due to lowering of the Li content. Moreover, the behaviour after 800 °C anneal is even more spectacular. The S parameter is not decreasing significantly from that of the 600 °C level, indicating that the defects are much more stable than vacancies and vacancy clusters which to a large degree anneal out at 800 °C in the High and Medium Li samples (comparing with Figures 4.5 and 4.6). The W(S) plot in Figure 4.7 shows large open volumes after 600 and 800 °C anneal as indicated by the strong deviation from the bulk-$V_{Zn}$ line. Even after 1000 °C anneal, the S parameter is above typical bulk values, indicating that the defects persist, but the W(S) plot show that the size of the open volumes has decreased. PAS measurements has also been performed in an experiment designed to reveal more of the nature of the polishing defects and a plot is shown in Appendix C that confirms that thermally stable defects are created by polishing. Selim *et al.* also observed an increase in S parameter after polishing, and attributed this to defects created by dislocating motions during the polishing procedure [67]. They reported that the defects annealed out at 1100 °C. Presumably the same defects introduced by polishing was also observed using PL by Hamby *et al.* [68] and was identified as $Zn_i$ and $V_{Zn}$, acting as donor and acceptor, respectively.

A mechanism that explains the annealing behaviour in Figure 4.7 can be proposed. The defects introduced by polishing are observed by PAS in the as-implanted sample, indicating that open volumes exist before annealing. These defects are thermally more stable than point defects introduced by for example ion implantation, indicating that the defects may

be dislocations. Annealing at 600 °C causes mobile vacancies created by the ion implantation to diffuse to the dislocations and become trapped. This causes large open volumes to be created, where the vacancies are bound with varying strength to the dislocations. When the temperature is increased, some vacancies dissociates and are allowed to diffuse and eventually anneal out causing a drop in the S parameter. However, the S parameter stays high compared with bulk values even after 1000 °C anneal, indicating that a major part of the dislocations are still present.

In addition to the PAS measurements, SIMS gave another indication of polishing induced damage. In Figure 4.4 an accumulation of Li can be seen in the region near the surface ($\leq 5\,\mu$m. deep) after annealing the Low Li sample. This accumulation is a result of highly mobile Li diffusing from the bulk and being trapped in defects near the surface. The defects in question here are not only related to implantation, since the defects penetrates much deeper than the projected range, and as such polishing damage is a likely cause. The Li level in the 800 °C sample falls below $10^{13}\,\mathrm{cm}^{-3}$, a concentration so low that it can be called depleted. Since the measurement was ended at about 18 $\mu$m, an estimate of how deep the Li depletion is can be made by assuming a constant Li concentration in the as-implanted sample and an abrupt end of the Li depleted region.

$$\int_0^{5\mu m} C_{800\,^\circ C}(x)\,\mathrm{d}x = \int_0^{a} C_{as-implanted}(x)\,\mathrm{d}x \tag{5.1}$$

By solving with respect to $a$, one finds that Li is depleted till a depth of $\sim 34\,\mu$m.

In Figure 4.4, the flank where the Li concentration is dropping dramatically in the 600 °C and 800 °C samples can be seen to be wider in the 800 °C sample, and dramatically wider in the 1000 °C sample. This may indicate that the complex created by Li and a trap is diffusing outward again from the area where Li was trapped, and this complex has a much lower diffusivity than Li in the bulk. It must be noted that the situation may be

more complex than sketched above, for instance several complexes having different dissociation properties may be involved.

# Chapter 6

# Conclusions and further work

## 6.1 Conclusions

$N^+$ ion-implantation into HT ZnO causes production of zinc vacancies ($V_{Zn}$) and small vacancy clusters detected using PAS. $V_{Zn}$ is an acceptor and the cause of a highly resistivity implantation induced layer located slightly before projected range, as detected by SSRM.

In the samples annealed at 600 °C, we observe formation of large vacancy clusters with 3-4 $V_{Zn}$ and probably a similar number of $V_O$. This effect is more pronounced in samples containing more Li, meaning that Li is an essential part of these vacancy clusters.

Indications of the electrical activation of nitrogen related acceptors are observed after annealing at several temperatures. Specifically a Li–N complex is suggested to be activated by 800 °C annealing. The Li–N complex is believed to be doubly negative because it is visible to positrons, in contrast to the other N related acceptors observed.

It was observed that Li accumulates in a region close to projected range. This region is damaged by ion-implantation and thus a high concentration of Li traps is found here. A simulation was performed and the result matches a selected diffusion profile reasonably well.

We discovered damages created by mechanical polishing that reached

deeper into the samples than expected. In this region PAS profiles were affected significantly, suggesting that this treatment is not suitable for experiments involving PAS. This finding is in agreement with a recent study by Selim *et al.* [67]. In addition we observe that the polishing induced damage acts as Li traps and causes accumulation of Li in the surface region. These traps, when filled with Li, has a much lower diffusivity than the Li present in bulk, and widening profiles can be seen with increasing annealing temperatures.

## 6.2 Suggestions for further work

The possible Li–N complex should be studied further, first and foremost to determine un-ambiguously its presence. Preferably such a study should be performed on single crystal samples of high quality containing negligible concentration of Li, for example vapor phase or melt grown ZnO. A method can then be developed to introduce Li by diffusion to obtain a controllable concentration in the range from $\sim 5 \times 10^{14}\,\mathrm{Li/cm^3}$ to $\sim 1 \times 10^{18}$. $5 \times 10^{14}\,\mathrm{Li/cm^3}$ is a quite low concentration, but still measurable by SIMS. With this method developed one could introduce varying concentrations of Li, including one substrate without any Li. Nitrogen could be introduced by ion-implantation, and annealing performed at 800 °C, which has previously caused activation of the acceptors visible by PAS. By measuring the samples with PAS and SIMS, one could then determine if the acceptor activation is purely N related or if Li plays an important part. In addition temperature dependent PAS studies and/or Hall measurements would be valuable to determine the activation energy of the possible complexes.

In addition, the diffusion constant of Li can be determined during development of the above mentioned method to introduce low concentrations of Li in pure ZnO crystals, and the subsequent isochronal or isothermal anneals. This way is more reliable than ion implantation, due to the complexity of implantation induced traps.

A study of the nature of the Li traps observed herein and whether they are O or Zn related can be performed. One could use low energy electron irradiation (100-500 keV) to produce defects in the sample. Because of the difference in mass between Zn and O, it is possible to selectively generate defects on only one sublattice as shown by Rempel *et al.* in SiC [69]. At energies below a certain threshold value, electron irradiation should create damage primarily on the O sublattice, thus creating $V_O$ and $O_i$. Above this threshold value, a more equal distribution of damage on both sublattices is expected. The concentration of Zn vacancies could be monitored using PAS. Li can then be introduced to the sample either by in-diffusion or ion-implantation of Li to achieve a concentration higher then the defect concentration created by the electron concentration, followed by annealing at relatively low temperatures so that the created defects does not anneal out, and Li is allowed to diffuse and fill the the potential defects acting as Li traps. One could then measure the Li concentration using SIMS and by comparing samples irradiated with different energy, one could determine if the traps are related to the O sublattice ($V_O$ and $O_i$) or Zn sublattice ($V_{Zn}$ and $Zn_i$).

# Appendix A

# Vacancy distribution as calculated by TRIM

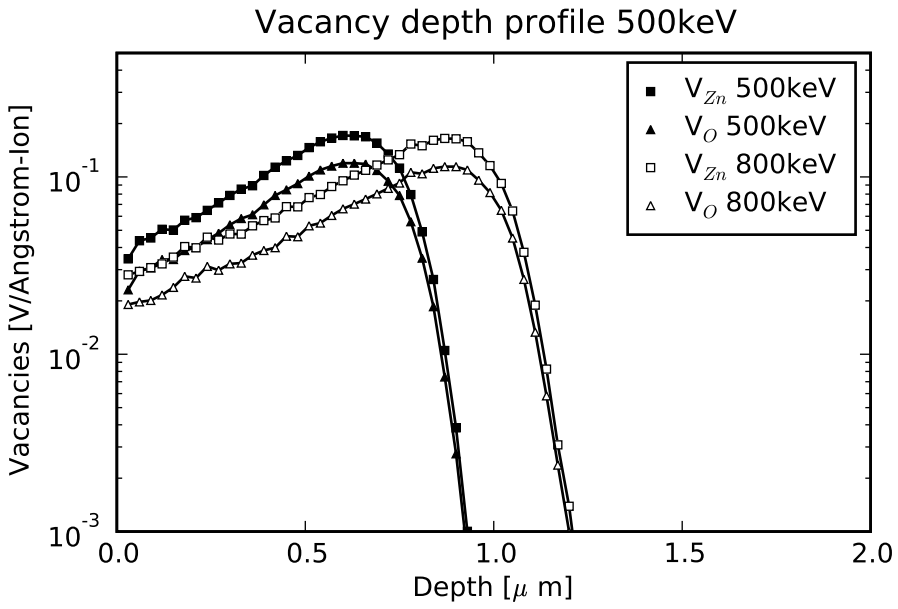


Figure A.1: *Vacancy depth profiles as calculated by TRIM using $N^+$ implantation energies of 500 keV and 800 keV. The unit on y-axis is the output from TRIM. Calibration is needed to convert this to concentration units.*

A simulation using TRIM was done to establish that peak $V_{Zn}$ concen-

tration created by $N^+$ implantation is the same whether 500 keV or 800 keV energy was used. The difference is only in the depth of the peak which is at ∼640 nm and ∼890 nm, respectively, as seen in Figure A.1.

# Appendix B

# Matlab code for Li diffusion and trapping

The matlab code listed below is a modification of a diffusion script written by Klaus Magnus Håland Johansen (e-mail: k.m.h.johansen@fys.uio.no).

```
% Setting the constants
D = 3e-12 %D0*exp(-Ea/(k_b*T)) %2.7e-11; %cm^2/s

v = 0.00;
R = 1e-8; %5e-8; %cm
K = 4*pi*R*D;

D = D*1e8; %Converting to um^2/s since the imported data is in um.
dx = 0.05;

Li = 5.3e16;

% Time step
dt=0.08*dx*dx/(2*D)
min = 60;
time_stop = min*60;

%Initial conditions
size = 30;
i_end = size/dx;

%Setting initial vector:
Peak1 = 6e17;
Pos1 = 0.78;
Wid1 = 0.14;
```

```
Peak2 = 0e17;
Pos2 = 0.1;
Wid2 = 0.03;

Peak3 = 0e17;
Pos3 = 0.05;
Wid3 = 0.01;

for i = 1:i_end

u1(1,i) = Li;
x(i) = dx*i;
Trap(1,i) = Peak1*exp(-(x(i)-Pos1)^2/Wid1)
 + Peak2*exp(-(x(i)-Pos2)^2/Wid2)
 + Peak3*exp(-(x(i)-Pos3)^2/Wid3);

end

% Preallocations
u1_temp = double(zeros(1,i_end-1));
u2 = double(zeros(1,i_end-1));
u2_temp = double(zeros(1,i_end-1));

%Boundary conditions
for n = 1:2%n_end
    %Li-concentration
    u1(1,1) = Li; %1e25;
    u1(1,i_end) = Li;

    %Complex-concentration
    u2(1,1)=0;
    u2(1,i_end)=0;
end

n = 0;
time = 0;

%Time iterations
while time < time_stop
    n = n + 1;

    %Position iteration
    for i = 2:i_end-1

        %Complex formation
        u2_temp(1,i) = (K*(u1(1,i))*abs(Trap(1,i)
```

```
          - u2(1,i)) - v*u2(1,i))*dt + u2(1,i);

        %Diffusion
        u1_temp(1,i) = dt*(D*(u1(1,i+1)-2*u1(1,i)+u1(1,i-1))/(dx*dx))
         - (K*(u1(1,i))*abs(Trap(1,i)-u2(1,i))-v*u2(1,i))*dt + u1(1,i);

        u1(1,i) = u1_temp(1,i);
        u2(1,i) = u2_temp(1,i);

        u1(1,1) = u1(1,2); %2*u1(1,2)-u1(1,3);
        u2(1,1) = u2(1,2); %2*u2(1,2)-u2(1,3);
    end

    time = time + dt;
end

% Plot
```

# Appendix C

# Polishing induced defects measured by PAS

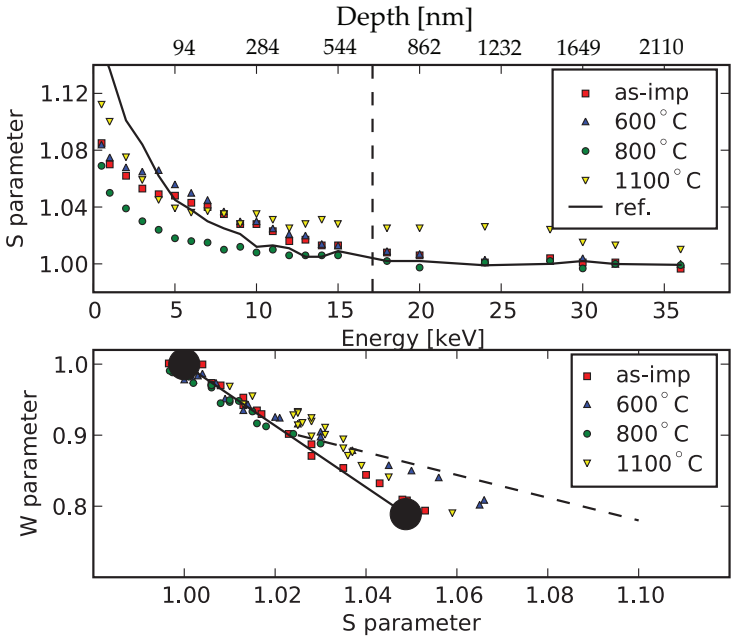


Figure C.1: *Positron annihilation spectroscopy results for samples polished and annealed at given temperatures. Top: S parameter vs Energy. Bottom: W parameter vs S parameter*

A set of samples was heat treated at 1500 °C and polished. Then the

samples was measured using PAS Doppler broadening spectroscopy. The results is illustrated in Figure C.1, and indicate that polishing induces a rather deep defect profile.

# Bibliography


[1] P. Zu, Z. K. Tang, G. K. L. Wong, M. Kawasaki, A. Ohtomo, H. Koinuma, and Y. Segawa. Ultraviolet spontaneous and stimulated emissions from ZnO microcrystallite thin films at room temperature. *Solid State Communications*, 103(8):459 – 463, 1997.

[2] D. M. Bagnall, Y. F. Chen, Z. Zhu, T. Yao, S. Koyama, M. Y. Shen, and T. Goto. Optically pumped lasing of ZnO at room temperature. *Applied Physics Letters*, 70(17):2230–2232, 1997.

[3] T. Makino, C. H. Chia, Nguen T. Tuan, Y. Segawa, M. Kawasaki, A. Ohtomo, K. Tamura, and H. Koinuma. Radiative and nonradiative recombination processes in lattice-matched (Cd,Zn)O/(Mg,Zn)O multiquantum wells. *Applied Physics Letters*, 77(11):1632–1634, 2000.

[4] A. Ohtomo, M. Kawasaki, T. Koida, K. Masubuchi, H. Koinuma, Y. Sakurai, Y. Yoshida, T. Yasuda, and Y. Segawa. $Mg_xZn_{(1-x)}O$ as a II–VI widegap semiconductor alloy. *Applied Physics Letters*, 72(19):2466–2468, 1998.

[5] T. Dietl, H. Ohno, and F. Matsukura. Hole-mediated ferromagnetism in tetrahedrally coordinated semiconductors. *Phys. Rev. B*, 63(19):195205, Apr 2001.

[6] J.J. Lander. Reactions of Lithium as a Donor and an Acceptor in ZnO. *J. Phys. Chem. Solids*, 15(2):324–34, 1960.

[7] D. B. Laks, C. G. Van de Walle, G. F. Neumark, and S. T. Pantelides. Role of native defects in wide-band-gap semiconductors. *Phys. Rev. Lett.*, 66(5):648–651, Feb 1991.

[8] D. C. Look, J. W. Hemsky, and J. R. Sizelove. Residual native shallow donor in ZnO. *Phys. Rev. Lett.*, 82(12):2552–2555, Mar 1999.

[9] D. C. Look, G. C. Farlow, Pakpoom Reunchan, Sukit Limpijumnong, S. B. Zhang, and K. Nordlund. Evidence for native-defect donors in *n*-type ZnO. *Physical Review Letters*, 95(22):225502, 2005.

[10] C.G. Van de Walle. Defect analysis and engineering in ZnO. *Physica B: Condensed Matter*, 308-310:899 – 903, 2001.

[11] T.M. Børseth, F. Tuomisto, J.S. Christensen, W. Skorupa, E.V. Monakhov, B.G. Svensson, and A.Y. Kuznetsov. Deactivation of Li by vacancy clusters in ion-implanted and flash-annealed ZnO. *Appl. Phys. Lett Phys Rev B*, 74:161202, 2005.

[12] T.M. Børseth, F. Tuomisto, J.S. Christensen, E.V. Monakhov, B.G. Svensson, and A.Y. Kuznetsov. Vacancy clustering and acceptor activation in nitrogen-implanted ZnO. *Physical Review B*, 77(4), 2008.

[13] X. H. Wang, B. Yao, Z. P. Wei, D. Z. Sheng, Z. Z. Zhang, B. H. Li, Y. M. Lu, D. X. Zhao, J. Y. Zhang, X. W. Fan, L. X. Guan, and C. X. Cong. Acceptor formation mechanisms determination from electrical and optical properties of p-type ZnO doped with lithium and nitrogen. *Journal of Physics D: Applied Physics*, 39(21):4568–4571, 2006.

[14] J. G. Lu, Y. Z. Zhang, Z. Z. Ye, L. P. Zhu, L. Wang, B. H. Zhao, and Q. L. Liang. Low-resistivity, stable p-type ZnO thin films realized using a Li–N dual-acceptor doping method. *Applied Physics Letters*, 88(22):222114, 2006.

[15] Y.Z. Zhang, J.G. Lu, Z.Z. Ye, H.P. He, L.L. Chen, and B.H. Zhao. Identification of acceptor states in Li–N dual-doped p-type ZnO thin films. *Chinese Physics Letters*, 26(4):046103 (4pp), 2009.

[16] Charles Kittel. *Introduction to Solid State Physics*. John Wiley and Sons, Inc, 8 edition, 2005.

[17] Ben G. Streetman and S. K. Banerjee. *Solid state electronic devices*. Prentice-Hall, Inc., Upper Saddle River, NJ, USA, 6 edition, 2005.

[18] F. Tuomisto, K. Saarinen, D. C. Look, and G. C. Farlow. Introduction and recovery of point defects in electron-irradiated ZnO. *Phys. Rev. B*, 72(8):085206, Aug 2005.

[19] Y. J. Zeng, Z. Z. Ye, W. Z. Xu, J. G. Lu, H. P. He, L. P. Zhu, B. H. Zhao, Y. Che, and S. B. Zhang. p-type behavior in nominally undoped ZnO thin films by oxygen plasma growth. *Applied Physics Letters*, 88(26):262103, 2006.

[20] A. Janotti and C.G. Van de Walle. Native point defects in ZnO. *Physical Review B*, 76(16):165202, 2007.

[21] F. A. Kroger. *The Chemistry of Imperfect Crystals*. North-Holland, Amsterdam, 1974.

[22] A. F. Kohan, G. Ceder, D. Morgan, and C. G. Van de Walle. First-principles study of native point defects in ZnO. *Physical Review B*, 61(22):15019–15027, Jun 2000.

[23] F. Oba, S.R. Nishitani, S. Isotani, H. Adachi, and I. Tanaka. Energetics of native defects in ZnO. *Journal of Applied Physics*, 90(2):824–828, 2001.

[24] F. Tuomisto, V. Ranki, K. Saarinen, and D C. Look. Evidence of the Zn vacancy acting as the dominant acceptor in *n*-type ZnO. *Phys. Rev. Lett.*, 91(20):205502, Nov 2003.

[25] A. Zubiaga, F. Tuomisto, V. A. Coleman, H. H. Tan, C. Jagadish, K. Koike, S. Sasa, M. Inoue, and M. Yano. Mechanisms of electrical isolation in $O^+$-irradiated ZnO. *Physical Review B (Condensed Matter and Materials Physics)*, 78(3):035125, 2008.

[26] N. H. Nickel and K. Fleischer. Hydrogen local vibrational modes in zinc oxide. *Phys. Rev. Lett.*, 90(19):197402, May 2003.

[27] J. Bang and K.J. Chang. Diffusion and thermal stability of hydrogen in ZnO. *Applied Physics Letters*, 92(13):132109, 2008.

[28] B.K. Meyer, H. Alves, D.M. Hofmann, W. Kriegseis, D. Forster, F. Bertram, J. Christen, A. Hoffmann, M. Strassburg, M. Dworzak, et al. Bound exciton and donor-acceptor pair recombinations in ZnO. *physica status solidi (b)*, 241(2), 2004.

[29] T. Minami, H. Sato, H. Nanto, and S. Takata. Group-III impurity doped zinc oxide thin films prepared by RF magnetron sputtering. *Japanese Journal of Applied Physics*, 24(Part 2, No. 10):L781–L784, 1985.

[30] C. G. Van de Walle, D. B. Laks, G. F. Neumark, and S. T. Pantelides. First-principles calculations of solubilities and doping limits: Li, Na, and N in ZnSe. *Phys. Rev. B*, 47(15):9425–9434, Apr 1993.

[31] W. Walukiewicz. Defect formation and diffusion in heavily doped semiconductors. *Phys. Rev. B*, 50(8):5221–5225, Aug 1994.

[32] Y. J. Zeng, Z. Z. Ye, W. Z. Xu, D. Y. Li, J. G. Lu, L. P. Zhu, and B. H. Zhao. Dopant source choice for formation of p-type ZnO: Li acceptor. *Applied Physics Letters*, 88(6):062107, 2006.

[33] Y. R. Ryu, T. S. Lee, and H. W. White. Properties of arsenic-doped p-type zno grown by hybrid beam deposition. *Applied Physics Letters*, 83(1):87–89, 2003.

[34] H.S. Kang, G.H. Kim, D.L. Kim, H.W. Chang, B.D. Ahn, and S.Y. Lee. Investigation on the p-type formation mechanism of arsenic doped p-type ZnO thin film. *Applied Physics Letters*, 89(18):181103, 2006.

[35] L. J. Mandalapu, Z. Yang, F. X. Xiu, D. T. Zhao, and J. L. Liu. Homojunction photodiodes based on Sb-doped p-type ZnO for ultraviolet detection. *Applied Physics Letters*, 88(9):092103, 2006.

[36] F. X. Xiu, Z. Yang, L. J. Mandalapu, D. T. Zhao, J. L. Liu, and W. P. Beyermann. High-mobility Sb-doped p-type ZnO by molecular-beam epitaxy. *Applied Physics Letters*, 87(15):152101, 2005.

[37] P. Wang, NuoFu Chen, and Z. G. Yin. P-doped p-type ZnO films deposited on Si substrate by radio-frequency magnetron sputtering. *Applied Physics Letters*, 88(15):152102, 2006.

[38] T. Aoki, Y. Hatanaka, and D.C. Look. ZnO diode fabricated by excimer-laser doping. *Applied Physics Letters*, 76(22):3257–3258, 2000.

[39] W. Liu, S. L. Gu, J. D. Ye, S. M. Zhu, S. M. Liu, X. Zhou, R. Zhang, Y. Shi, Y. D. Zheng, Y. Hang, and C. L. Zhang. Blue-yellow ZnO homostructural light-emitting diode realized by metalorganic chemical vapor deposition technique. *Applied Physics Letters*, 88(9):092101, 2006.

[40] A. Tsukazaki, A. Ohtomo, T. Onuma, M. Ohtani, T. Makino, M. Sumiya, K. Ohtani, S.F. Chichibu, S. Fuke, Y. Segawa, et al. Repeated temperature modulation epitaxy for p-type doping and light-emitting diode based on ZnO. *Nature Materials*, 4(1):42–46, 2004.

[41] J. G. Lu, Z. Z. Ye, F. Zhuge, Y. J. Zeng, B. H. Zhao, and L. P. Zhu. p-type conduction in N–Al co-doped ZnO thin films. *Applied Physics Letters*, 85(15):3134–3135, 2004.

[42] Z. Y. Xiao, Y. C. Liu, R. Mu, D. X. Zhao, and J. Y. Zhang. Stability of p-type conductivity in nitrogen-doped ZnO thin film. *Applied Physics Letters*, 92(5):052106, 2008.

[43] C. H. Park, S. B. Zhang, and Su-Huai Wei. Origin of p-type doping difficulty in ZnO: The impurity perspective. *Phys. Rev. B*, 66(7):073202, Aug 2002.

[44] A. Zeuner, H. Alves, DM Hofmann, BK Meyer, A. Hoffmann, U. Haboeck, M. Strassburg, and M. Dworzak. Optical Properties of the Nitrogen Acceptor in Epitaxial ZnO. *physica status solidi (b)*, 234(3), 2002.

[45] T. Maqsood. Hydrothermal ZnO; mastering of Lithium content and formation of Palladium Schottky diodes. Master's thesis, University of Oslo, July 2008.

[46] A. Onodera, N. Tamaki, Y. Kawamura, T. Sawada, and H. Yamashita. Dielectric activity and ferroelectricity in piezoelectric semiconductor Li-doped ZnO. *Japanese Journal of Applied Physics*, 35(Part 1, No. 9B):5160–5162, 1996.

[47] Z. Q. Chen, M. Maekawa, and A. Kawasuso. Energy variable slow positron beam study of $Li^+$-implantation-induced defects in ZnO. *Chinese Physics Letters*, 23(3):675–677, 2006.

[48] R. M. Park, M. B. Troffer, C. M. Rouleau, J. M. DePuydt, and M. A. Haase. p-type ZnSe by nitrogen atom beam doping during molecular beam epitaxial growth. *Applied Physics Letters*, 57(20):2127–2129, 1990.

[49] H. D. Jung, C. D. Song, S. Q. Wang, K. Arai, Y. H. Wu, Z. Zhu, T. Yao, and H. Katayama-Yoshida. Carrier concentration enhancement of p-type ZnSe and ZnS by codoping with active nitrogen and tellurium by using a delta-doping technique. *Applied Physics Letters*, 70(9):1143–1145, 1997.

[50] D.C. Look, D.C. Reynolds, C.W. Litton, R.L. Jones, D.B. Eason, and G. Cantwell. Characterization of homoepitaxial p-type ZnO grown by molecular beam epitaxy. *Applied physics letters*, 81:1830, 2002.

[51] M. Komatsu, N. Ohashi, I. Sakaguchi, S. Hishita, and H. Haneda. Ga, N solubility limit in co-implanted ZnO measured by secondary ion mass spectrometry. *Applied Surface Science*, 189(3-4):349 – 352, 2002.

[52] K. Iwata, P. Fons, A. Yamada, K. Matsubara, and S. Niki. Nitrogen-induced defects in ZnO:N grown on sapphire substrate by gas source MBE. *Journal of Crystal Growth*, 209(2-3):526 – 531, 2000.

[53] E.C. Lee, Y.S. Kim, Y.G. Jin, and K.J. Chang. Compensation mechanism for N acceptors in ZnO. *Phys. Rev. B*, 64(8):085120, Aug 2001.

[54] L. Li, C.X. Shan, B.H. Li, B. Yao, J.Y. Zhang, D.X. Zhao, Z.Z. Zhang, D.Z. Shen, X.W. Fan, and Y.M. Lu. The compensation source in nitrogen doped ZnO. *Journal of Physics D: Applied Physics*, 41:245402, 2008.

[55] Z. Q. Chen, M. Maekawa, A. Kawasuso, R. Suzuki, and T. Ohdaira. Interaction of nitrogen with vacancy defects in $N^+$-implanted ZnO studied using a slow positron beam. *Applied Physics Letters*, 87(9):091910, 2005.

[56] X.Y. Duan, R.H. Yao, and Y.J. Zhao. The mechanism of Li, N dual-acceptor co-doped p-type ZnO. *Applied Physics A: Materials Science & Processing*, 91:467–472, June 2008.

[57] A. Ore and J. L. Powell. Three-photon annihilation of an electron-positron pair. *Phys. Rev.*, 75(11):1696–1699, Jun 1949.

[58] A. Vehanen, K. Saarinen, P. Hautojärvi, and H. Huomo. Profiling multilayer structures with monoenergetic positrons. *Phys. Rev. B*, 35(10):4606–4610, Apr 1987.

[59] N. Duhayon, P. Eyben, M. Fouchier, T. Clarysse, W. Vandervorst, D. Alvarez, S. Schoemann, M. Ciappa, M. Stangoni, W. Fichtner, et al. Assessing the performance of two-dimensional dopant profiling techniques. *Journal of Vacuum Science & Technology B: Microelectronics and Nanometer Structures*, 22:385, 2004.

[60] P. Eyben. *Scanning spreading resistance microscopy : High resolution two-dimensional carrier profiling of semiconductor structures*. PhD thesis, Katholieke Universiteit Leuven, 2004.

[61] M. Winter. Isotopes of lithium. Website, April 2009. `http://www.webelements.com/lithium/isotopes.html`.

[62] J.F. Ziegler. Srim-2003. *Nuclear Instruments and Methods in Physics Research Section B: Beam Interactions with Materials and Atoms*, 219-220:1027 – 1036, 2004. Proceedings of the Sixteenth International Conference on Ion Beam Analysis.

[63] J. Lindhard, M. Scharff, and H.E. Schiøtt. Range concepts and heavy ion ranges. *Matematisk-fysiske Meddelelser Det Kongelige Danske Videnskabernes Selskab*, 33(14):1–42, 1963.

[64] R. A. Brown, O. Kononchuk, G. A. Rozgonyi, S. Koveshnikov, A. P. Knights, P. J. Simpson, and F. González. Impurity gettering to secondary defects created by MeV ion implantation in silicon. *Journal of Applied Physics*, 84(5):2459–2465, 1998.

[65] H.T. Yuan, Z.Q. Zeng, Z.X. Mei, X.L. Du, J.F. Jia, and Q.K. Xue. Surfactant effects of lithium dopant during molecular beam epitaxy of ZnO films. *Journal of Physics: Condensed Matter*, 19(48):482001, 2007.

[66] K.M. Johansen, J.S. Christensen, E.V. Monakhov, A.Yu. Kuznetsov, and B.G. Svensson. Deuterium diffusion and trapping in hydrothermally grown single crystalline ZnO. *Applied Physics Letters*, 93(15):152109, 2008.

[67] F.A. Selim, M.H. Weber, D. Solodovnikov, and K.G. Lynn. Nature of native defects in ZnO. *Physical review letters*, 99(8):085502, 2007.

[68] D. W. Hamby, D. A. Lucca, and M. J. Klopfstein. Photoluminescence of mechanically polished ZnO. *Journal of Applied Physics*, 97(4):043504, 2005.

[69] A. A. Rempel, W. Sprengel, K. Blaurock, K. J. Reichle, J. Major, and H.-E. Schaefer. Identification of lattice vacancies on the two sublattices of SiC. *Phys. Rev. Lett.*, 89(18):185501, Oct 2002.